SAND2021-11617

SANDIA REPORT
SAND20XX-XXXX
Printed Click to enter a date

Sandia National Laboratories

Integrated Multiphysics Modeling of Environmentally Assisted Brittle Fracture

Jessica M. Rimsza, Reese E. Jones, Jeremy E. Trageser, Joshua H. Hogancamp, Christa E. Torrence, Cody Mitts, Chven Mitchell, Mahmoud Reda Taha, Patience Raby, Richard A. Regueiro, Dhafer Jadaan

Prepared by
Sandia National Laboratories
Albuquerque, New Mexico
87185 and Livermore,
California 94550

Issued by Sandia National Laboratories, operated for the United States Department of Energy by National Technology & Engineering Solutions of Sandia, LLC.

Available to DOE and DOE contractors from
U.S. Department of Energy
Office of Scientific and Technical Information
P.O. Box 62
Oak Ridge, TN 37831

Telephone: (865) 576-8401
Facsimile: (865) 576-5728
E-Mail: reports@osti.gov
Online ordering: http://www.osti.gov/scitech

Available to the public from
U.S. Department of Commerce
National Technical Information Service
5301 Shawnee Rd
Alexandria, VA 22312

Telephone: (800) 553-6847
Facsimile: (703) 605-6900
E-Mail: orders@ntis.gov
Online order: https://classic.ntis.gov/help/order-methods/

ABSTRACT

Brittle materials, such as cement, compose major portions of built infrastructure and are vulnerable to degradation and fracture from chemo-mechanical effects. Currently, methods of modeling infrastructure do not account for the presence of a reactive environment, such as water, on the acceleration of failure. Here, we have developed methodologies and models of concrete and cement fracture that account for varying material properties, such as strength, shrinkage, and fracture toughness due to degradation or hydration. The models have been incorporated into peridynamics, non-local continuum mechanics methodology, that can model intersecting and branching brittle fracture that occurs in multicomponent brittle materials, such as concrete. Through development of new peridynamic capabilities, decalcification of cement and differential shrinkage in clay-cement composites have been evaluated, along with exemplar problems in nuclear waste cannisters and wellbores. We have developed methods to simulate multiphase phenomena in cement and cement-composite materials for energy and infrastructure applications.

ACKNOWLEDGEMENTS

We would like to thank David Littlewood, Jennifer Fredrick, and Tara LaForce for technical input and discussion early in the project. This work is supported by the Laboratory Directed Research and Development Program at Sandia National Laboratories.

CONTENTS

1. Introduction 11
2. Accomplishments 14
   - 2.1. Journal Articles 14
     - 2.1.1. Published 14
     - 2.1.2. Submitted 14
     - 2.1.3. In Progress 14
   - 2.2. Post-Docs and Students 14
     - 2.2.1. Post-Docs 14
     - 2.2.2. Interns 14
     - 2.2.3. Graduate Students 14
   - 2.3. Conference Presentations 15
     - 2.3.1. 2019 15
     - 2.3.2. 2020 15
     - 2.3.3. 2021 16
   - 2.4. Other Presentations/Documentation 16
     - 2.4.1. 2019 16
     - 2.4.2. 2020 16
     - 2.4.3. 2021 16
3. Peridynamics Methodology 17
   - 3.1. Standard Formulation 17
   - 3.2. Peridigm Developments 18
4. Decalcification Fracture Model 20
   - 4.1. Overview 20
   - 4.2. Methods 20
   - 4.3. Results 21
   - 4.4. Conclusions 23
5. Fracture from Differential shrinkage 25
   - 5.1. Overview 25
   - 5.2. Methods 26
   - 5.3. Results 27
   - 5.4. Conclusions 28
6. Concrete fracture in exemplar geometries 29
   - 6.1. Hydration of Dual-Purpose Cannister Cement Filler 29
   - 6.2. Wellbore Microannulus 32
7. CZ Modeling of Concrete Hydration 39
8. Cement Paste Durability 41

LIST OF FIGURES

Figure 1-1. (top left) Fracture in the Pacoima Dam during Northridge Earthquake [3], (top right) External damage of a concrete building following the 7.1 Magnitude earthquake in Mexico City on Sept. 19, 2017 (Buchanan, Lee, Pecanha, and Lai, The New York Times, 2017), (bottom) Breaching failure due to a close-in explosion of 6000 kg TNT equivalent [4] 11

Figure 1-2. (a) schematic of well bore casing (SAND2017-13229C) (b) schematic of well bore seals [1] (c) schematic of fractures in solid (left) and heterogenous (right) quartz from 13
Figure 4-1: Linear model used for degradation of OPC properties [47].....20
Figure 4-2. Support starting to buckle (t = 7.2 months, 8.4 months, 9.6 months) after being subjected to chemical attack at a point midway on the right side. Support is colored by the damage field (blue: 1.0, red: 0.0). Note that surfaces (existing and newly created) are colored blue since particles there have lower coordination than in the interior of the beam. [47].....22
Figure 4-3. Local (secant) and global (variance) primary (first order) sensitivities of time to fracture and failure to the selected material properties. Local sensitivities are given in years. Global sensitivities are non-dimensional. Ref: [47] 23
Figure 4-4. Uncertainty of time to fracture and failure: (a) joint distribution, and (b) marginal distributions. Note that the normalized distributions are in units of (1/year). Ref: [47].....23
Figure 5-1. Snapshots of three cement (grey) – clay (red) cylindrical model geometries with (left) a single clay sphere, (middle) four separated clay spheres, and (right) distributed clay. 27
Figure 6-1. Geometry of cement cylinder sample with 45% porosity.....29
Figure 6-2. Cracking in phosphate cement from simulated shrinkage. Visualized in a cross section to show the internal cracks formed during shrinkage. 30
Figure 6-3. Cracking in phosphate cement from simulated expansion. Visualized in a cross section to show the internal cracks from expansion. 31
Figure 6-4. Shrinkage cracks forming in a phosphate cement cylinder, seen here in a cross section to show the internal cracks.....31
Figure 6-5. Simplified wellbore geometry for evaluation of role of microannulus. 32
Figure 6-6. FE mesh and corresponding peridynamic material points for modeling wellbore geometries. 33
Figure 6-7. Cross-section of peridynamic wellbore problem description.....34
Figure 6-8. Geometries of microannulus geometries in peridynamics borehole simulations.....35
Figure 6-9. Damage variation for quarter (A), half (B), and full (C) microannulus geometries. 36
Figure 6-10. Schematic of wellbore model for extended lifetime failure and includes subsurface rock, cement sheath, and steel casing. 37
Figure 6-11. Damage propagation in wellbore models as time progresses t = 125, 250, 365 days (left to right).....38
Figure 8-1. Schematic representation of the four primary forms of cement degradation: chloride penetration, carbonation, calcium leaching, and sulfate attack [69].....41
Figure 8-2. (a) Schematic and (b) test setup of cement paste fracture test using three-point bending. 42
Figure 8-3. Degradation environment a) bath with no samples. b) and c) Two degradation baths for calcium leaching and sulfate attack with samples. 43
Figure 8-4. Samples degradation at different exposure time showing the significance of degradation on the external color and appearance of cement paste. 43
Figure 8-5. Summary data for modulus of elasticity, modulus of rupture, and fracture energy after 12-weeks of exposure to degrading environment.....44

LIST OF TABLES

Table 4-1. Nominal values and ranges of material properties for cement paste with water/cement ratio (W/C) 0.4–0.5 and aged 28 days. Poisson's ratio is fixed at 0.25 by the numerical formulation and change in reaction rate is estimated by the change of surface area via the change of porosity using a fixed decalcification rate per surface area. [47] 21

Table 6-1. Aluminum phosphate cement properties [65] used in peridynamics simulations 29
Table 6-2. Cement and steel properties for peridynamic wellbore simulations. [66] 32
Table 6-3. Steel, cement, and subsurface rock properties and failure criteria used in peridynamic simulations of wellbores with subsurface rock [66].....37

This page left blank

EXECUTIVE SUMMARY

Brittle materials, such as cement, compose major sections of infrastructure and external stresses and aging causes vulnerabilities. During exposure to aqueous conditions, environmentally assisted crack growth can occur, and models that include chemical impacts can provide insight into structural reliability. One such modeling methodology is peridynamics, a state-of-the-art mechanics theory developed at Sandia National Laboratories for capturing material failure. Peridynamics is a nonlocal extension of classical solid mechanics that is well-suited to handle spatial discontinuities such as crack formation and fracture. It is distinct from classical continuum mechanics because integral equations, rather than partial derivatives are used, which eliminates mathematical difficulties associates with crack-tip singularities. The application of peridynamics to built infrastructure applications required model development and here we have added a degradation model, varying interface properties, and material shrinkage. Additionally, a weakly coupled thermomechanical model, a dynamic relaxation solver, and a bond softening damage model were developed, based on challenges with time scales and dynamic processes.

These peridynamic developments were implemented in multiple applications. First, decalcification of cement was investigated for evaluation of the decrease in material strength and fracture properties with exposure to aqueous conditions. The model included fundamental aspects of degradation of cement, including softening, reduced toughness, and shrinkage of the cement and increased reactivity and transport with water induced degradation. The model was calibrated to existing experimental data using simulations of common tests such as flexure, compression, and diffusion. Global sensitivity and uncertainty of predicted failure times were calculated based on variation of eleven fundamental material properties. Strong sensitivities to the diffusion coefficient, the reaction rate, and shrinkage with degradation were identified.

Following successful evaluation of the impact of decalcification of cement on fracture and failure times, a cement-clay composite material was evaluated during dehydration. The clay-cement system serves as an exemplar for the impact of differential shrinkage on the fracture properties. Three different geometries were evaluated, a cement cylinder containing a single clay sphere, a cement cylinder containing four clay spheres, and 20% clay evenly distributed throughout the cement. Comparing computational modeling with experimental results identified that cement shrinkage and strength control the resulting fractures, while the strength of the clay and the clay-cement interface have only a minimal effect. Therefore, it is the properties of the supporting material (cement) that controls the resulting fracture.

Two additional exemplar problems were investigated, including wellbore integrity and hydration of cement filler for dual-purpose canisters. Evaluation of the role of microcannulas between the steel and cement regions identifies weakness points along the borehole, while hydration of cement filler causes fracturing due to shrinkage, resulting in external water intrusion. Evaluation of these exemplar cases using the newly developed peridynamic techniques are discussed and shed light into how aging of cementitious materials can impact new and existing energy infrastructure.

Finally, work by two external collaborators, Dr. Richard Regueiro from University Colorado Boulder and Dr. M. Reda Taha at the University of New Mexico are discussed. Dr. Regueiro's group implemented cohesive zone modeling of cement fracture and Dr. Taha's group experimentally evaluated the changes in cement strength during decalcification and sulfate exposure. Through evaluation of a suite of cement-based applications, peridynamic models that captures both environmental and physical effects of cement fracture are captured, resulting in the development of a multiphysics model of fracture for energy infrastructure applications.

ACRONYMS AND DEFINITIONS

Abbreviation	Definition
2D	Two-Dimensional
CH	Calcium Hydroxide
CIE	Cohesive Interface Element
CZ	Cohesive Zone
DFN	Discrete Fracture Networks
DOE	Department of Energy
DPCs	Dual Purpose Cannisters
FEA	Finite Element Analysis
FEM	Finite Element Method
HCP	Hardened Cement Paste
LEFM	Linear Elastic Fracture Mechanics
OPC	Ordinary Portland Cement
QoIs	Quantities of Interest
SNF	Spent Nuclear Fuel
TGA	Thermal Gravimetric Analysis
UCS	Unconfined Compressive Strength
UEL	User Element
UQ	Uncertainty Quantification

1. INTRODUCTION

Brittle materials such as cement compose major sections of infrastructure, and external stresses from either man-made threats or natural disasters can cause vulnerabilities. Following structural failures that caused significant loss of life (9/11 Terror Attacks, Minnesota Bridge Collapse), structures are now engineered to minimize the likelihood of collapse. This results in buildings that have survived an event but have sustained damage. During exposure to aqueous conditions, environmentally assisted crack growth can further destabilize the structures, and models that predict chemical impacts can provide insight into structural reliability. As an example, the US Department of the Interior released a history of eleven concrete dams, and identified fractures in the foundation, bedrock, or the face of the dams following natural disasters (earthquake, flooding) that required stabilization. [2] See Figure 1-1.

Figure 1-1. (top left) Fracture in the Pacoima Dam during Northridge Earthquake [3], (top right) External damage of a concrete building following the 7.1 Magnitude earthquake in Mexico City on Sept. 19, 2017 (Buchanan, Lee, Pecanha, and Lai, The New York Times, 2017), (bottom) Breaching failure due to a close-in explosion of 6000 kg TNT equivalent [4]

A critical factor in the evaluation of infrastructure reliability is the role of the environment on fracture growth. Due to the small flaw size that can lead to catastrophic failure in brittle materials [5] the inspection, evaluation, and design of current structures needs to be supported by both a fundamental science understanding of failure mechanisms and structurally relevant models that can provide guidelines for failure under varying conditions.

Currently, probabilistic models are often used to assist in uncertainty quantification (UQ) in lifetime prediction of infrastructures systems, [6] and rely on the selection of key variables to predict material performance. [7] Probabilistic models do not include specifics of the fracture process nor the flow of water into existing fractures, which limit their application. Additionally, cohesive zone (CZ) models have been extensively applied for the explicit modeling of cement/concrete fracture through a combination of linear elastic fracture mechanics (LFEM) and finite element methods (FEM). [8] [9] CZ modeling methods have been successful in describing fracture of cement systems and inclusion of the process zone and to our knowledge environmental effects, including changes in fracture properties under aqueous conditions have not been included. [10-14]

Within the geosciences, simulation of water flow and fracture occurs in large reservoir-scale discrete fracture network (DFN) modeling [15] with deformation added through FEM. [16] Water

flow through DFNs has been incorporated into existing models [17] but does not account for advancing fractures. Generally, available codes perform either DFN modeling or fluid flow, and when water is incorporated the interaction between the network and the water occurs through bulk variables, such as hydraulic pressure, flow rate, and stresses [18]. Examples include FracMan with discrete fracture data analysis and flow and transport modeling, ROCMAS which uses FEM for coupled flow and stress analysis of fractured rocks [19], FEHM a continuum model for pore fluid flow, heat transfer, and deformation [16], and AltaStim, a stochastic fracture and flow software [20]. Additionally, reservoir modeling is at an entirely different scale than the infrastructure problems, and opportunities exist to use a higher fidelity model, which incorporates some of the explicit physics and chemistry associated with fracture growth. Therefore, the development of modeling methodology that operates at infrastructure scale, includes fracture growth through chemo-mechanical effects, and can simulate branching and intersecting fracture is necessary. One such methodology is peridynamics.

Peridynamics is a state-of-the-art mechanics theory developed at Sandia National Laboratories specifically for capturing material failure. Peridynamics is a nonlocal extension of classical solid mechanics that is well-suited to handle spatial discontinuities such as crack formation and fracture. It is distinct from classical continuum mechanics because integral equations, rather than partial derivatives, are used, which eliminates mathematical difficulties associates with crack-tip singularities. [21, 22] One open-source code used for peridynamics modeling is called Peridigm. The meshless discretization utilized by Peridigm excels at modeling the evolution of complex fracture geometries. Mechanical behavior and material failure are captured using nonlocal interactions between a material point and its neighbors over a region called the horizon. [23] Material failure is modeled by altering or eliminating the interaction between material points. The critical-stretch failure law, for instance, dictates that material point interactions are broken when the distance between the points exceeds a specified limit, which is a function of the material properties (fracture energy release rate). [21] The net result is a modeling framework with several key advantages over a LEFM approach allowing for simulation of (i) fracture branching and initiation [24, 25], (ii) interaction and coalescence of fractures [26], and (iii) fracture of composites or heterogenous systems. [27, 28]

The peridynamics methodology has been validated with experiments for controlled geometries [25, 29] and compared with alternative fracture models. [29, 30] Peridynamics models have been implemented for applications in concrete structures, [31-33] projectile impacts, [34] and fiber reinforced composites [35] and has been incorporated with both molecular dynamics [36] and finite element analysis (FEA) frameworks. [34, 37] Water has been introduced into the peridynamics framework for applications in hydrofracking. [30] In previous investigations, the water pressure is the driver of crack growth, [26] rather than explicit chemical reactivity of the water with the surrounding solid, which dominates at slower strain rates. [38]

Here, several different multiple exemplar problems were used to develop peridynamic modeling of environmentally assisted fracture. These include the decalcification of cement for evaluation of aging infrastructure and the role of differential shrinkage of fracture of cement-clay structures. Further targeted applications include wellbore integrity and hydration of cement filler for

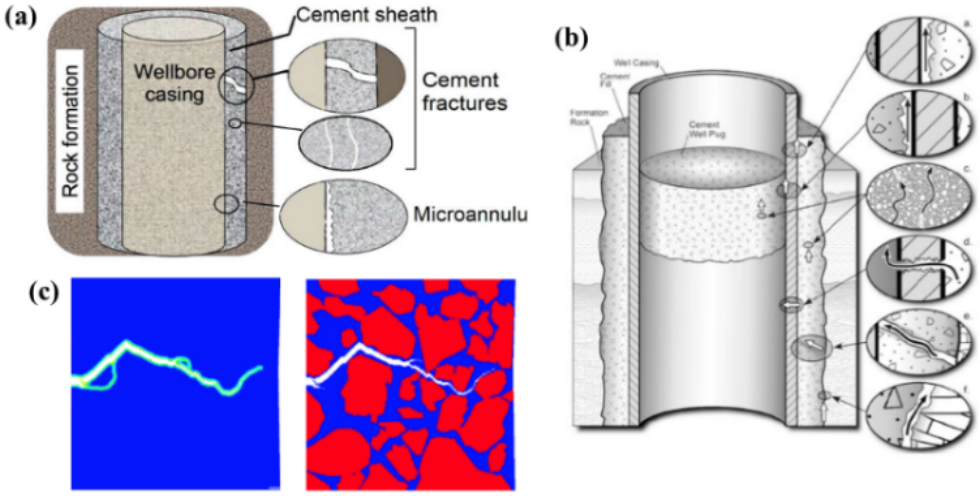

dual-purpose canisters (DPCs). Wellbores are formed as part of the recovery of natural resources, and more recently as a component in the underground storage of CO_2 [39]. Wellbore failure is expensive to repair and has cost lives, with "cementing" reported as a factor in ~50% of well blow outs in the Gulf of Mexico. [40] See examples of wellbore failures in Figure 1-2. Wellbore casing is used as a model geometry for investigation of environmentally assisted fracture by looking at different locations of fracture initiation along the wellbore and how that impacts further cracking of the casing. Results would also be transferable to tunnel based structures, including storm drains [41] and illicit/covert tunnels. [42]

Spent nuclear fuel (SNF) requires disposal by the U.S. Department of Energy (DOE) and is currently stored in DPCs [43]. Filler materials for DPCs that mitigates criticality during disposal are being considered, including phosphate-based cements. Here, the role of variation in phosphate-based cement properties as a function of water content is evaluated during the cement setting phase. This includes the role of shrinkage and porosity in causing fracturing that impacts the integrity of the filler material. The results are transferable to other applications of solid cement phases, such as bridge supports.

Through the incorporation of environmental effects into fracture modeling, the ability to predict fracture of large-scale infrastructure projects will be significantly improved and result in a more realistic physics-based understanding of functional lifetimes. The resulting simulation tool has significantly expanded the application space of Peridigm, supporting the homeland security and energy mission space of Sandia National Laboratories.

Figure 1-2. (a) schematic of well bore casing (SAND2017-13229C) (b) schematic of well bore seals [1] (c) schematic of fractures in solid (left) and heterogenous (right) quartz from

2. ACCOMPLISHMENTS

This section provides a list of published materials produced from this project. Links to published journal articles and SAND numbers are provided when possible to provide the reader access.

2.1. Journal Articles

2.1.1. Published

Jones, R. E., Rimsza, J. M., Trageser, J. E., & Hogancamp, J. R. (2021). Simulation of hardened cement degradation and estimation of uncertainty in predicted failure times with peridynamics. *Construction and Building Materials*, *286*, 122927. SAND2021-3950J
https://www.sciencedirect.com/science/article/pii/S0950061821006875

2.1.2. Submitted

Raby, P, Rimsza, J.M., Stormont, J. & Taha, M. M. Reda. (2021) Cement Degradation Methods: A Comparative Review.

2.1.3. In Progress

Torrence, C.E., Trageser, J.E., Hogancamp, J., Jones, R.E., and Rimsza, J.M. (2021) Sensitivity Analysis of Concrete's Interfacial Transition Zone (ITZ) Strength and Toughness Using Peridynamics.

Trageser, J.E., Mitchell, C.A., Rimsza, J.M., Pyrak-Nolte, L.J., Jones, R.E., & Matteo, E.N. (2021) Effect of Differential Shrinkage on Crack Formation

Jadaan, D., Raby, P., Jones, R.E., Taha, M.R., Rimsza, J.M., & Regueiro, R. (2021) Phenomenological Mode-I Cohesive Zone Elastoplastic Model of Crack Strengthening and Weakening due to Chemistry

Jadaan, D., Jones, R.E., Rimsza, J.M., & Regueiro, R. (2021) Poromechanical Cohesive Interface Element with Simple Combined Mode I-II Cohesive Zone Elastoplasticity for Simulating Fracture in Saturated Porous Media

2.2. Post-Docs and Students

2.2.1. Post-Docs

Christa E. Torrence – Christa has a PhD in Civil Engineering from Texas A&M University. Her primary focus was on identifying the role of the interfacial transition zone (ITZ) on concrete properties using peridynamics.

2.2.2. Interns

Cody Mitts (University of Arizona) – Cody is a PhD student in Aerospace and Mechanical Engineering at the University of Arizona working with Dr. Erdogan Madenci. His project was on the identifying weaknesses in wellbore geometries and the influence of changing critical stretch description in peridynamics on the fracture properties of cement paste.

2.2.3. Graduate Students

Dhafer Jadaan (University of Colorado Boulder) – Dhafer completed a PhD in Civil, Environmental, and Architectural Engineering at University of Colorado Boulder working with Dr. Richard Regueiro. His dissertation was on the development of CZ modeling methodologies for modeling of cement

fracturing with varying water pore-pressures. This work was supported by Campus Executive LDRD funding.

Patience Raby (University of New Mexico) – Patience completed a MS in the Department of Civil, Construction and Environmental Engineering working with Dr. Mahmoud Reda Taha. Her thesis investigated the role of calcium leaching and sulfate attack on the strength of ordinary Portland cement (OPC) paste.

Chven Mitchell (Purdue University) – Chven is a PhD student in the Department of Earth, Atmospheric, and Planetary Science at Purdue University working with Dr. Laura Pyrak-Nolte. Her collaborative work including experimental evaluation of cement fracture with varying clay inclusions, which was modeled using peridynamics for this project.

2.3. Conference Presentations

2.3.1. 2019

Rimsza, J.M., Jones, R.E., LaForce, T., & Littlewood, D. (2019) Modeling of multiphysics crack growth in cement with peridynamics simulations. *10th Advances in Cement Based Materials* SAND2019-2850A, SAND2019-6838C

Jones, R.E., Rimsza, J.M, Littlewood, D. & LaForce, T. (2019) Modeling multiphysics crack growth in cement. *56th Annual Technical Meeting of the Society of Engineering Science (SES2019)* SAND2019-10360A SAND2019-13255C

Invited - Littlewood, D.J., Rimsza, J.M., Fredrick, J., & Jones, R.E. (2019) Coupled peridynamic and subsurface flow models for environmentally assisted crack growth in concrete structures. *SIAM Conference on Computational Science and Engineering* SAND2018-9663A

2.3.2. 2020

Rimsza, J.M. Trageser, J.E., Hogancamp, J.R., & Jones, R.E. (2020) Modeling of multiphysics crack growth in cement with peridynamic simulations. *11th Advances in Cement Based Materials* SAND2020-3160A – cancelled due to COVID-19 pandemic

Raby, P., Rimsza, J.M., & Taha, M.M. Reda. (2020) Effect of relative humidity on cement cracking and fracture. *Concreep 11*+ SAND2020-1503A – cancelled due to COVID-19 pandemic

Trageser, J.E., Mitchell, C.A.M, Pyrak-Nolte, L.J., & Rimsza, J.M. (2020) Evaluation of fracture in cement-clay systems through application of non-local peridynamics. *2020 American Geophysical Union Fall Meeting* SAND2020-7645A SAND2020-12824C

Rimsza, J.M., Trageser, J., Jones, R.E., Mitchell, C.A.M., & Pyrak-Nolte, L.J. (2020) Modeling drying of cement-clay composites with non-local peridynamics. *2020 American Geophysical Union Fall Meeting* SAND2020-12851C SAND2020-7529A

Pyrak-Nolte, L.J., Jiang, L., Mitchell, C., Xu, Z., Cao, Hongfan, C., Yoon, S., Kang, P.K., Rimsza, J.M., Trageser, J.E., Bobet, A., and Yoon, H. (2020) Rock-Fluid Interactions: Fracture Formation and Fluid Distributions. *2020 American Geophysical Union Fall Meeting* SAND2020-7651A

Trageser, J, Jones, R.E., Rimsza, J.M., & Hogancamp, J. (2020) Modeling degradation in concrete via peridynamics. *IMECE International Mechanical Engineering Congress & Exposition* SAND2020-10348C

2.3.3. 2021

Raby, P., Stormont, J., Rimsza, J.M., & Taha, M.M. Reda (2021) Cracking and fracture of cement exposed to calcium leaching. *Biot-Bažant Conference* SAND2021-0035A

Torrence, C.E., Jones, R.E., Trageser, J.E., & Rimsza, J.M. (2021) Determination of influential parameters on concrete fracture using peridynamics. *12th Advances in Cement Based Materials* SAND2021-7155C

2.4. Other Presentations/Documentation

2.4.1. 2019

Rimsza, J.M. Peridynamics + PFLOTRAN coupling for predicting cement fracture in aqueous conditions. (2019) *9th Sandia Earth Science Symposium* SAND2019-5070D

2.4.2. 2020

Rimsza, J.M. Resiliency of Degraded Built Infrastructure. (2020) *White Paper* SAND2020-9615R

Rimsza, J.M. Peridynamics modeling of cement fracture during degradation. (2020) *10th Sandia Earth Science Symposium* SAND2020-5034PE

2.4.3. 2021

Torrence, C.E. Relationships between concrete morphology and fracture behavior. (2021) *11th Sandia Earth Science Symposium* SAND2021-6180PE

3. PERIDYNAMICS METHODOLOGY

3.1. Standard Formulation

Peridynamics is a non-local formulation of continuum mechanics where the continuum is represented by a finite set of material points. A key feature of peridynamics is the lack of spatial derivatives in the governing equations. This feature avoids difficulties arising from discontinuities such as fracture.

There are two main formulations of peridynamics, the general state-based peridynamics [44] and the simpler subcase, bond-based peridynamics [21]. This work focuses on bond-based peridynamics wherein each material point interacts directly with material points within a region about the material point called the neighborhood. Although not required, the neighborhood is typically taken as the set of points within a fixed distance, called the horizon, of the material point. In the reference configuration, a material point is assumed to have a connection called a *bond* to every material point in its neighborhood. Bonds are permitted to break irreversibly according to a maximum stretch criterion. When bonds break, their load is transferred to surrounding points and can result in the progressive breakage of bonds. The broken bonds represent damage within the material.

The integro-differential reformulation of the balance of moment

$$\rho(\boldsymbol{x})\ddot{\boldsymbol{u}}(\boldsymbol{x},t) = \int_{\mathcal{H}_x} \boldsymbol{f}\big(\boldsymbol{u}(\boldsymbol{x}',t),\boldsymbol{u}(\boldsymbol{x},t),\boldsymbol{x}',\boldsymbol{x}\big)\, dV_{\boldsymbol{x}} + \boldsymbol{b}(\boldsymbol{x},t) \tag{1}$$

is the governing equation of motion in bond based peridynamics where $\rho(\boldsymbol{x})$ is the mass density at material point **x**, $\ddot{\boldsymbol{u}}$ is the second derivative in time of the displacement field $\boldsymbol{u}$, $\mathcal{H}_x$ is the neighborhood of **x**, **f** is the pairwise force function describing the influence material point **x**' exerts on material point **x**, and **b** is a prescribed body force density field. We employ a shorthand:

$$\boldsymbol{\xi} := \boldsymbol{x}' - \boldsymbol{x} \quad and \quad \boldsymbol{\eta} := \boldsymbol{u}(\boldsymbol{x}',t) - \boldsymbol{u}(\boldsymbol{x},t) \tag{2}$$

Here we use the prototype microelastic brittle model [21] where the force function **f** is described by

$$\boldsymbol{f}\big(\boldsymbol{u}(\boldsymbol{x}',t),\boldsymbol{u}(\boldsymbol{x},t),\boldsymbol{x}',\boldsymbol{x}\big) := cs(t,\boldsymbol{\eta},\boldsymbol{\xi})\mu(t,\boldsymbol{\xi})\frac{\xi+\eta}{|\boldsymbol{\xi}+\boldsymbol{\eta}|} \tag{3}$$

where c is a material dependent constant,

$$s(t,\boldsymbol{\eta},\boldsymbol{\xi}) := \frac{|\boldsymbol{\xi}+\boldsymbol{\eta}| - |\boldsymbol{\xi}|}{|\boldsymbol{\xi}|} \tag{4}$$

is the stretch in the bond between **x** and **x**', and

$$\mu(t,\boldsymbol{\xi}) := \begin{cases} 1, & if\ s\big(t',\boldsymbol{\eta},\boldsymbol{\xi}\big) < s_0 \quad \forall t' \le t \\ 0, & else \end{cases} \tag{5}$$

is a history-dependent binary-valued function the describes whether a bond is intact or broken based on a critical stretch (s_0). The material parameters c and s_0 are material dependent, and for convenience they are typically related to commonly measured material parameters. The parameter c in Equation (6) is typically associated with an elastic constant; however, in classical linear elasticity the model is described by two engineering constants such as Poisson's ratio and the bulk modulus (K). Due to the use of a pairwise force function in bond-based peridynamics only materials nearly satisfying Cauchy's relations are able to be described. [45] In the case of isotropy, Cauchy's relations reduce to a fixed Poisson's ratio of $\frac{1}{4}$. [46] The parameter c is then related to K through the relation:

$$c = \frac{18k}{\pi\delta^4} \tag{6}$$

where δ is the horizon. The s_0 is frequently related to the fracture energy (G_0) through the relation:

$$s_0 = \sqrt{\frac{5G_0}{8k\delta}} \tag{7}$$

3.2. Peridigm Developments

During the project, several improvements were added to Peridigm based on the scientific needs of the project. These changes are outlined below. For access and methods of implementation, please contact Jeremy Trageser (jtrages@sandia.gov)

Degradation Model: The implemented degradation model allows the material properties (density, elastic modulus, fracture toughness) to vary from an initial to a final state based on a single variable. In our initial case, the variable with concentration of calcium in an OPC material. As an example, a linear model was used with end points of a "pristine" and a "degraded" state variable. Here c = 1 is for the pristine case and c = 0 for the degraded case. For elastic stiffness (E) the resulting function is:

$$E = E_1 + (E_0 - E_1)(1 - c) \tag{8}$$

With E_1 as the pristine value of the Young's modulus, E_0 as the degraded value and c as an evaluation of the amount of degradation. The same methodology is used for all other variables in the system including fracture toughness, compressive strength, volumetric stretch, diffusivity, and water reaction rates. Additionally, other material properties can be varied similarly based on the specific model investigated. For further description of the model, see Ref: [47]

Varying Interfacial Material Properties: In the standard version of Peridigm, material properties between two different materials were an average of the material property in each material. For example, in a cement-clay mixture, the bulk modulus of the interface would be 15.5 GPa, an average of the value for cement (20.0 GPa) and hydrated clay (11.0 GPa). Since interfaces are known to be weaker than the surrounding material, this modification allows for varying of the properties of these interfacial regions specifically.

Incorporation of Shrinkage into Elastic Models: Along with varying mechanical and fracture properties, hydration process can result in volumetric changes as well. By modifying the stress-free reference configuration, we introduced shrinkage/expansion into a peridynamic model. In this case a variable, c, is used to describe the progression of the drying front through the material. The shrinkage parameter, α, is then introduced to describe the overall change in volume.

Weakly Coupled Thermomechanical Model: In the implemented model, first the parameter described by diffusion (e.g. moisture content, temperature, etc.) is solved for with the diffusion solver and then the mechanic solver is run with the degradation parameter previously mentioned dependent on the parameter described by diffusion.

Dynamic Relaxation Solver: A known concern with Peridigm has been failure of the quasistatic solver once bonds in the material started breaking. To avoid this issue, a damped explicit Velocity Verlet solver was implemented. This allows for the approximation of the quasi-static solution at each time step and reach beyond the initial fracture nucleation. This was critical for investigation of differential shrinkage in clay-cement systems that were computationally expensive and would not have been possible with the initial quasi-static solver in Peridigm.

Bond Softening Damage Model: The initial Peridigm methodology included a stepwise bond breakage conditions, where once a critical stretch length was reached, the bond would fail completely and immediately. In some cases, this led to failure that was faster than predicted initially. In this model, rather than a bond breaking after reaching a critical stretch, it instead softens after it reaches its peak

and then eventually breaks if it keeps stretching. The type of softening can also be controlled and used to tune post-fracture behavior.

4. DECALCIFICATION FRACTURE MODEL

4.1. Overview

Modeling the degradation of cement-based infrastructure due to aqueous environmental conditions is an ongoing challenge. To develop a modeling capability to predict built infrastructure failure due to chemical degradation, we created a chemo mechanical model of the effects of long-term water exposure on cement. The model couples the mechanical static equilibrium balance with reactive–diffusive transport and incorporates fracture and failure via peridynamics. The model includes fundamental aspects of degradation of OPC paste, including the observed softening, reduced toughness, and shrinkage of the cement paste, and increased reactivity and transport with water induced degradation. This version of the model focuses on the first stage of cement paste decalcification, the dissolution of portlandite. Given unknowns in the cement paste degradation process and the cost of UQ, we adopt a minimally complex model in two-dimensions (2D) to perform sensitivity analysis and UQ. The model was calibrated to existing experimental data using simulations of common tests such as flexure, compression, and diffusion. The global sensitivity and uncertainty of predicted failure times was calculated based on variation of eleven material properties. Strong sensitivities to the diffusion coefficient, the reaction rate, and the shrinkage with degradation were identified. Also, the predicted time of first fracture is correlated with the time to total failure in compression, which implies fracture can indicate impending degradation induced failure. Extension of the model to include the multiple reactions that describe complete degradation, viscous relaxation, post-peak load mechanisms, and to three dimensions is straightforward and ongoing.

4.2. Methods

We developed a chemo-mechanical model of the main phenomenological effects of water induced degradation of hardened cement paste (HCP), including softening, weakening, swelling, increased fluid transport and increased reactivity. The model couples the mechanical static equilibrium balance with reactive–diffusive transport and incorporates large-scale fracture and failure. Using a variety of analytic solutions to 2D boundary value problems emulating common mechanical and reaction–diffusion tests, the model was calibrated to experimental property measurements from the initial stage of HCP degradation, decalcification of calcium hydroxide. A linear model is used for each parameter for each parameter are used to describe change in material properties with degradation, described by the variable c. See relevant equations in Figure 4-1. Details on the implementation of the model are in the published manuscript, Ref: [47] Material properties for the pristine and degraded cement paste are included in Table 4-1.

$$
\begin{aligned}
&\text{Young's modulus } E && = \bar{E} + \Delta E\,(1 - \underline{c}) \\
&\text{Fracture toughness } K_{\text{Ic}} && = \bar{K}_{\text{Ic}} + \Delta K_{\text{Ic}}\,(1 - \underline{c}) \\
&\text{Compressive strength } \sigma_{\text{c}} && = \bar{\sigma}_{\text{c}} + \Delta \sigma_{\text{c}}\,(1 - \underline{c}) \\
&\text{Volumetric stretch } \vartheta && = 1 + \Delta \vartheta\,(1 - \underline{c}) \\
&\text{Diffusivity } D && = \bar{D} + \Delta D\,(1 - \underline{c}) \\
&\text{Reaction rate } K && = \bar{K} + \Delta K\,(1 - \underline{c})
\end{aligned}
$$

Figure 4-1: Linear model used for degradation of OPC properties [47]

Table 4-1. Nominal values and ranges of material properties for cement paste with water/cement ratio (W/C) 0.4–0.5 and aged 28 days. Poisson's ratio is fixed at 0.25 by the numerical formulation and change in reaction rate is estimated by the change of surface area via the change of porosity using a fixed decalcification rate per surface area. [47]

Property	Symbol	Pristine	Degraded
Young's Modulus (GPa)	E	30	3-19
Poisson's Ratio	V	0.25	-
Fracture Toughness (MPa-cm$^{1/2}$)	K_{IC}	2.8	1.8-2.3
Compressive Strength (MPa)	σ_c	35	21-33
Diffusivity (cm^2/yr)	D	1.4	5.8-28.5
Reaction Rate (1/yr)	K	22	47-66
Volumetric Shrinkage	α	0.0	0.0056-0.0066
Porosity	p	0.25	0.38-0.80

4.3. Results

The initial model was calibrated for the peridynamic stiffness parameter, the critical stretch value using the point spacings and the peridynamics horizon using a flexural test specimen. Transport, shrinkage, and reactivity where all also calibrated with varying model geometries. The shrinkage parameter was found to have a significant impact on the mechanical response, and multiple shrinkage values were evaluated. See Refence [47], Section 4.1 for a detailed description of the calibration procedure.

Following calibration, a sensitivity analysis was performed using two quantities of interest (QoIs) as (i) the time to first bond breakage and (ii) the time to total failure, when the structure becomes unstable. A simplified simulation of a bridge support was used, which is composed of a vertical 4 cm x 24 cm simply supported beam under static load that pre-compresses the beam to 10% of failure at nominal strain. See the geometry in Figure 4-2. The geometry includes a point source of water halfway up the model.

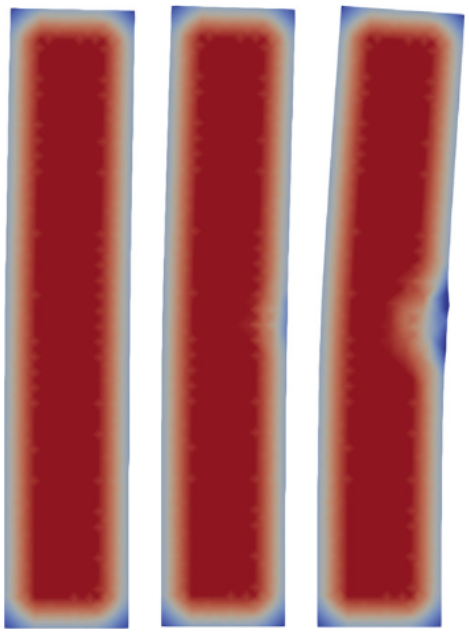

Figure 4-2. Support starting to buckle (t = 7.2 months, 8.4 months, 9.6 months) after being subjected to chemical attack at a point midway on the right side. Support is colored by the damage field (blue: 1.0, red: 0.0). Note that surfaces (existing and newly created) are colored blue since particles there have lower coordination than in the interior of the beam. [47]

Using this geometry, sensitivities are evaluated using an upper versus a lower bound for selected parameters while all other values are fixed at their median values. These sensitivities are based on decomposition of the variance of the outputs of the QoIs. Variance based sensitivities are included in Figure 4-3. Over 240,000 independent simulations were performed to identify the sensitivities. Overall, the chemical and transport parameters are more influential than the mechanical parameters given the respective uncertainties. Additionally, as indicated in the evaluation of the flexural test study, shrinkage is overall the dominant effect. Also, variations in the changes with degradation of the mechanical properties, such as fracture toughness and elastic modulus, have a greater effect on the time to fracture and failure. Additional uncertainty analysis indicated that time to fracture and the time to failure are strongly correlated and that there is significant variance in the outcome. See Figure 4-4. The average time to fracture is 2.9 months and time to failure is 8.2 months. The strong correlation indicates that the initial fracture is indicative of impending failure. Despite the overlap in these distributions the difference in the QoIs indicated that there would be nearly six months, or at least one month, of warning time prior to failure. A complete discussion of the details and implementation of the model can be found in publication, methodologies of the sensitivity and uncertainty analysis, and a more in-depth discussion is included in Reference: [47]

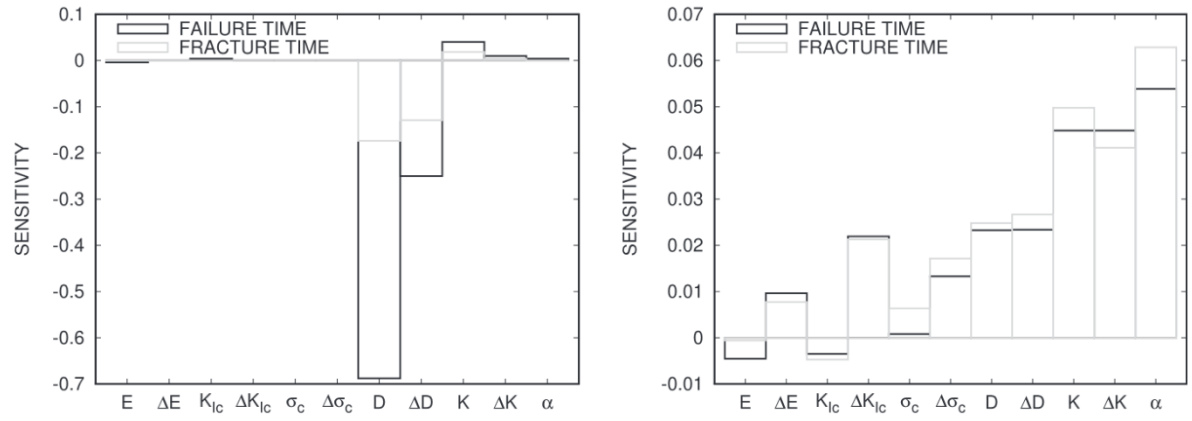

(a) local secant based (b) global variance based

Figure 4-3. Local (secant) and global (variance) primary (first order) sensitivities of time to fracture and failure to the selected material properties. Local sensitivities are given in years. Global sensitivities are non-dimensional. Ref: [47]

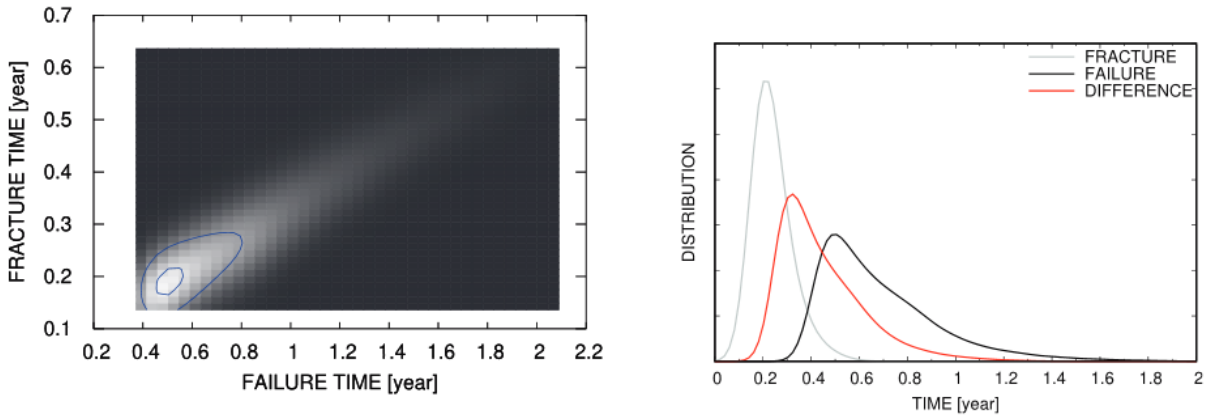

(a) (b)

Figure 4-4. Uncertainty of time to fracture and failure: (a) joint distribution, and (b) marginal distributions. Note that the normalized distributions are in units of (1/year). Ref: [47]

4.4. Conclusions

We demonstrated that the model is capable of plausible predictions of long-term failure of cement-based structures. The flexural bending and compressive beam failure results indicate high sensitivity to shrinkage and competing mechanisms for weakening of the HCP. UQ of eleven distinct parameters and their cross terms were investigated. Even with the simplified physical model we presented, the sensitivity analysis shows complex interplay of mechanisms and reemphasizes the importance of UQ in predictions of long-term behavior. Time-to-fracture and time-to-failure generally indicated to have a strong sensitivity to shrinkage, moderate sensitivity to reaction and transport properties, and lower sensitivities to mechanical properties, given the assumed uncertainties in these experimentally measured parameters and the model. The simulations indicated that initial fractures can be indications of imminent failure due to the strong correlation between these events and the time between these events being at least a significant fraction of a year. Despite the complexity, there are

numerous limitations of the present model due to simplifying assumptions and lack of experimental data, particularly: lumping the mobile species, ignoring precipitation, and the qualitative treatment of the post-peak load and diffusion front behavior. Modeling the post-peak load with more fidelity is straight-forward and can be accomplished by adding a non-zero post-rupture response to the bond force function, albeit with the cost of additional calibration parameters. In future work, we intend to pursue this enhancement and to extend the model to explore the interactions of complex fracture patterns evoked by more realistic geometry and directly represented with peridynamics.

5. FRACTURE FROM DIFFERENTIAL SHRINKAGE

5.1. Overview

Application of non-swelling clay minerals as a supplemental cementitious material to substitute cement clinker in concrete has been investigated as a method of reducing the carbon foot print of traditional concrete materials, [48] to improve green strength properties of self-compacting concrete [49], and to control autogenous shrinkage during cement drying [50]. Clay-cement mixtures have also been explored as analogs for clay bearing rocks and as proxies for the evaluation of the stability of host rocks for underground nuclear waste repositories [51]. Generally, the incorporation of clay into cement mixtures decreases the mechanical properties and hinders moisture transport when compared to pure OPC due to the weakness of pure clay systems and refined pores in blended cement-clay structures [48]. Incorporating some types of clay into cement can promote secondary chemical affects, for example when pozzolanic clay products such as metakaolin are mixed into the structure. Metakaolin exhibits a unique amorphous structure and is highly reactive when it is activated in alkali solutions that alters the properties of the final cement mixture [52].

When non-pozzolanic clay products such as montmorillonite are incorporated with cement mixtures, a decrease in the amount of autogenous deformation during cement setting may be observed [50]. The unique structure of non-calcified montmorillonite clay creates an environment for interesting interactions between the elements in the fluid and the clays, and intriguing chemo-mechanical behavior related to the contraction and expansion abilities. Experiments using neutron imaging have identified increases in porosity at the clay-cement interface, these enhanced porosity zones are related to the preferential portlandite dissolution at the boundary of the two materials [53]. In comparison to experimental work, modeling studies have focused on the thermodynamic properties of cement-clay mixtures to evaluate the impact on the stability of underground repositories [54-56]. For instance, thermodynamic modeling is generally accompanied by dissolution and precipitation kinetics of clay-cement structures [57, 58].

With the results of thermodynamic structures and dissolution and precipitation reactions, reactive transport investigations across the clay-cement interface have also been performed [59]. We have focused on the incorporation of non-calcinated clays in cement mixtures and the stability of the material post-formation, rather than chemical reactions that control the formation of the cement mixture or concrete. Investigations of the emergence of fractures in cement mixtures or concrete, particularly related to the presence of clay is uncommon, especially regarding the analysis of distributed clay-cement composites rather than clay-cement interfaces. Exceptions include the application of bonded elastic-plastic modeling of cement-improved clay, or cement-clay mixtures designed to improve the bonding and stability of cementitious soils [60]. Additionally, the role of clay swelling on fracturing has been explored using both discrete element method modeling [61] and FEM [62]. Ultimately, non-calcified clay as a control on fracture nucleation and damage propagation during dehydration of cement mixtures, to the best of our knowledge has been unexplored in literature. Therefore, peridynamics is employed to investigate fracturing in clay-cement composites during dehydration. Here, experimental and simulation methods are used to investigate three different cement mortar structures that contain either (i) a single clay inclusion, (ii) four clay inclusions, or (iii) clay distributed throughout the mortar. Peridynamics simulations are employed to investigate the influence of clay and cement shrinkage, interface strength, and the location of clay on the properties that control damage. To identify the critical factors that drive fracture nucleation and damage propagation in clay-cement materials, simulation results are compared to experimental data.

5.2. Methods

Samples for dehydration were experimentally fabricated using OPC, Ottawa sand, and commercial acid-activated Montmorilonite K10, a layered aluminosilicate powder. [57] All specimens were molded using cylindrical silicone molds of radius ~ 19.05 mm and length ~ 76.5 mm. Baseline samples containing OPC 3/15 only and OPC mortar were created along with three additional structures (i) a sample with one clay sphere, (ii) four clay bodies randomly distributed, and (iii) 20% clay distributed throughout the cylindrical framework. After molding, all geo-architected samples were cured in a hot water bath at 30◦C for seven days, then dehydrated within the X-Ray Microscope for six full days. Drying experiments were conducted with a Zeiss Xradia 510 Versa X-Ray Microscope on unbounded cylindrical geo-architected rock specimens. The synthetic rock samples were imaged at a pixel edge length resolution of ~ 40 μm at the start of the monitoring period to visualize the initial state of the framework at the onset of drying. All non-connected voids with volumes greater than 0.0005 mm^3 are considered in the estimation of total porosity. The unconfined compressive strength (UCS) of undrained samples were obtained for companion samples of each specimen at the onset of the monitoring period. Samples were placed at the center of the loading system and mounted between two steel plates.

Computational methods used here are consistent with the peridynamic model outlined in Section 3.1. with the Shrinkage Model from Section 3.2. The geometric structures utilized in the numerical experiments were selected to reflect the structure in the experimental geo-architectured rock samples. The numerical experiments were all cylinders with radius 19.05 mm and height 76.2 mm. The base material, mortar, is a homogeneous background and clay is incorporated in three different geometries. The first two geometries are mortar with a single clay inclusion and mortar with four clay inclusions. In order to produce realistic clay inclusions, each particle in the discretization was labeled based on the closest point in the experimental data. This was accomplished by segmenting the experimental data, so each point was associated with either mortar or clay and then labeling each particle in the discretization based on a nearest neighbor search over points in the experimental data. The last geometry we consider is an analogue of the distributed clay example. Unfortunately, the experimental data was not able to resolve the clay particles in the mortar. Instead, the numerical experiment randomly distributed clay spheres of radius 0.3 mm so that approximately 20% of the particles in the discretization are clay. See snapshots in Figure 5-1.

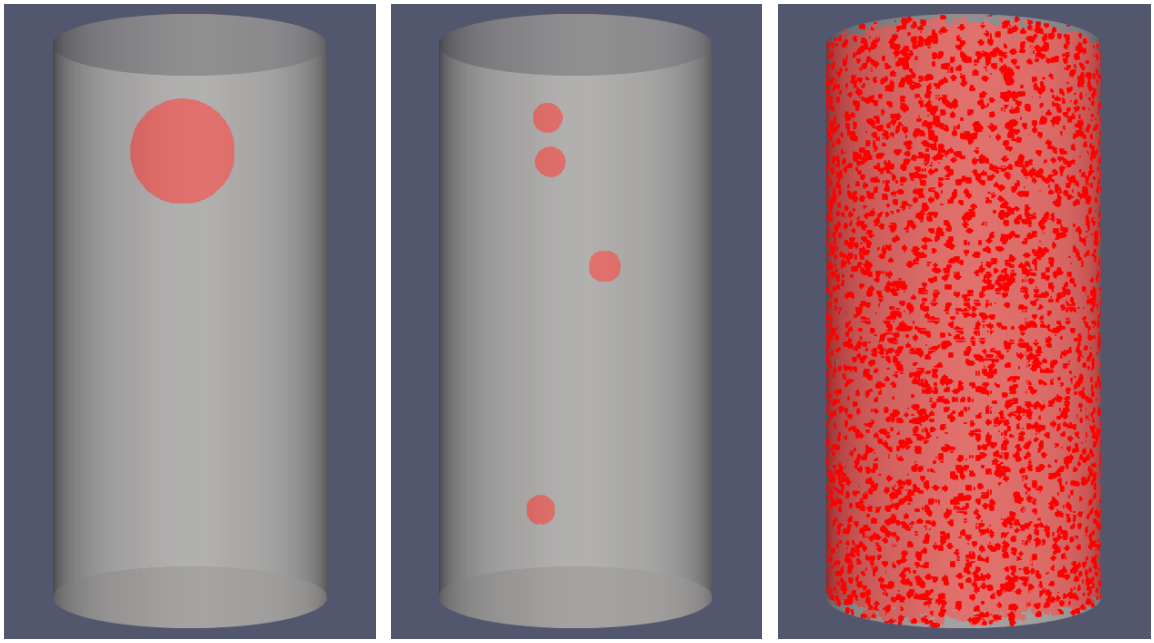

Figure 5-1. Snapshots of three cement (grey) – clay (red) cylindrical model geometries with (left) a single clay sphere, (middle) four separated clay spheres, and (right) distributed clay.

5.3. Results

The formation of discontinuities is exacerbated by the addition of montmorillonite to cement mortar mix. The addition of pre-soaked swelling clay increased the drying shrinkage and weakened the strength of the mortar framework. This is evident by the reduction in the UCS upon addition of swelling clay, which decreases from an average of 11.41 MPa, by 5% when multiple clay balls were added to the background matrix, by 47% when a single ball of clay is added, and by 64% when the montmorillonite is distributed throughout the specimen. Additionally, dimensional, and structural changes were observed in the localized and distributed clay samples. For the structure where clay is localized within the mortar framework, fractures or discontinuities are only observed where clay bodies exist. In samples with one or multiple localized clay spheres, the single clay ball experiences 26% shrinkage and the multiple embedded clay features experience on average of 83% volume loss per localized sphere. The final structures exhibit voids and cracks within the clay that are generated after debonding and shrinkage. No fractures are observed in the sample without clay. All samples with clay contained discontinuities that occurred as a result cracking, debonding at the mortar-clay interface, fracturing, and cracking within the individual inclusions as the water moves out of the cylindrical framework. The nucleation of fractures and propagation of the crack network is strongly dependent on the initial moisture condition, moisture loss behavior, and the length of time cured which relates to the initial moisture condition and strength of the sample.

Simulating damage propagation and nucleation is often a challenge due to a lack of regularity in the solution and the domain. Heterogeneity in the material, such as clay inclusions in a mortar matrix, creates further complications. To overcome these issues in the numerical experiments presented here, a novel thermomechanical peridynamics model was employed, where drying is simulated with a nonlocal diffusion process. Several of the characteristics of the experiments were replicated with numerical experiments. Overall, the addition of clay was found to weaken the mortar framework and encouraged the formation of discontinuities. In the numerical experiments where no

clay is present no fracturing occurs. This compares well with experimental results. The numerical experiments with localized clay inclusions produced fracture patterns localized within and around the clay bodies. In the distributed clay numerical experiments, the fracture network extends from the surface of the structure and arrests away from the boundary of the cylinder surface. Varying the parameters in the numerical experiments for mortar, a single clay inclusion, and four clay inclusions does not produce significantly different fracture patterns within the mortar matrix. On the other hand, several parameters were found to have profound effects on the fracture network that develops during drying in the distributed clay geometry. In particular, the clay and mortar shrinkage parameters have a dominant effect on the amount of fracture. The critical stretch parameter, which is related to the fracture energy, had a strong effect when varied for material points in the mortar and a marginal effect when varied in the clay or across the interface of the mortar and clay. This is likely due to the fracture energy of the clay and the interfaces being significantly lower than the mortar and the majority of shrinkage occurring in the clay. Another parameter producing a strong effect in the resulting fracture is the diffusivity parameter.

5.4. Conclusions

Differential shrinkage in clay-mortar systems was used to evaluate the role of varying shrinkage properties on fracture rates. By evaluating a suite of simulation parameters (cement/clay strength, cement/clay shrinkage, and water diffusion in clay/cement) several factors were found to have the biggest impact on the fracture pattern. The shrinkage of the cement and clay had the biggest impact, followed by the cement strength, and speed of water diffusion through the clay. These values had the largest variation and the biggest impact on the overall stress state of the matrix material. In comparison, the strength of the clay and the clay-cement interface had minimal impact on the fracture pattern since these features fail first in the material. Additionally, water diffusion in the cement had only a minimal impact since water diffusion in cement is already extremely slow. Overall, clay-cement mixtures exhibit unit fracture properties due to the strength and shrinkage differences, which results in a variation in the fracture patterns.

6. CONCRETE FRACTURE IN EXEMPLAR GEOMETRIES

6.1. Hydration of Dual-Purpose Cannister Cement Filler

Nuclear power plants in the United State produced thousands of metric tons of SNF, which requires disposal by the U.S. DOE. Currently SNF is stored in DPCs that are not designed for long-term disposal. [43] Due to concerns with the stability of DPCs, several approaches are being considered, one of which is to fill the void space of a DPC with a material that limits criticality during disposal. A filler material designed to mitigate criticality requires several attributes, including minimal volume reduction (< 10%) after infiltration and solidification [63]. Sandia National Laboratories is focusing on chemically bonded phosphate cements since encapsulation of radioactive water is a potential major application for this and similar materials [64]. Experimentally, five different cementitious materials were evaluated including, aluminum phosphate cements, calcium phosphate cements, magnesium potassium phosphate cements, fly ash phosphate cements, and wollastonite aluminum phosphate cements. Further down election based on setting times and workability has focused the results on aluminum phosphate-based cement, including the control of pore size via the addition of fillers [65]. Question remain regarding the amount of fracturing due to intrinsic porosity and shrinkage during setting and hydration will need to be considered during application. Therefore, peridynamics simulation of aluminum phosphate-based cements were undertaken, using the new shrinkage modeling capabilities (see Section 3.2).

A cylinder 75 mm tall with a 75 mm diameter with 45% porosity was generated. The cylinder is composed of 270,433 nodes arranged in a face centered cubic lattice pattern, correlating to a node spacing of 1.17 mm. The porosity was added by randomly selecting 45% of the nodes to be removed, resulting in a cylinder made of 148,738 nodes. An example is seen in Figure 6-1 with material properties included in Table 6-1.

Figure 6-1. Geometry of cement cylinder sample with 45% porosity

Table 6-1. Aluminum phosphate cement properties [65] used in peridynamics simulations

Property	Value	Units
Bulk Modulus	1	GPa
Fracture Toughness	1.5	$MPa \cdot m^{-1/2}$
Density	2	g/cm^3
Porosity	45	%

Property	Value	Units
Shrinkage	1	%

A spatially and time dependent temperature field is applied, where temperature is an analog for how much the cement has cured. As the cement sets, the external surfaces cure and dry at a faster rate than the interior of the sample. To represent this, in the simulation as the temperature rises, the nodes constrict inwards. Figure 6-2 shows cracks forming from the exterior of the cylinder towards the center.

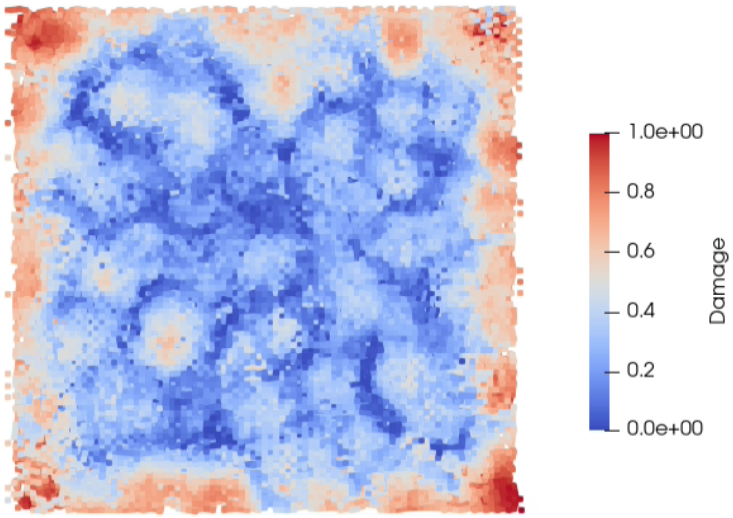

Figure 6-2. Cracking in phosphate cement from simulated shrinkage. Visualized in a cross section to show the internal cracks formed during shrinkage.

Some phosphate cement mixes have been shown to expand as they cure. Figure 6-3 shows the internal cracking resulting from an applied expansive field. The cracks are internal in this case, as the outer surface nodes pull on the internal nodes as they expand away from the center of the cylinder. Shrinkage cracking also occurs, see in Figure 6-4.

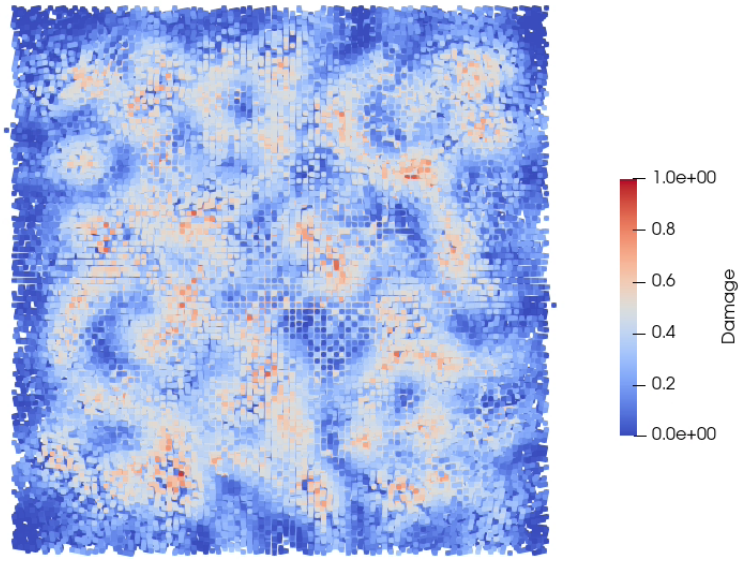

Figure 6-3. Cracking in phosphate cement from simulated expansion. Visualized in a cross section to show the internal cracks from expansion.

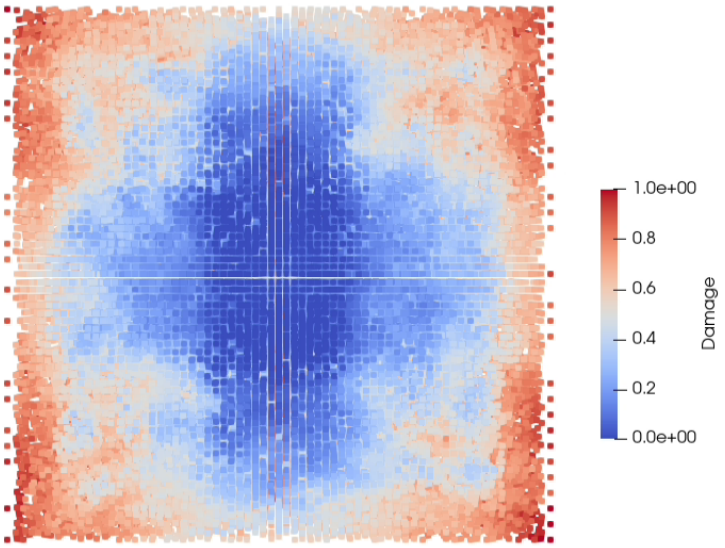

Figure 6-4. Shrinkage cracks forming in a phosphate cement cylinder, seen here in a cross section to show the internal cracks

Future work includes looking at the influence of pore size and pore size distribution on shrinkage cracking. Images of shrinkage cracking on laboratory samples are available for comparison and validation of the simulations. We will also look at the impact of the elastic modulus on the fracture patterns and amount of shrinkage-stress induced fracture, as the modulus varies with the composition, curing conditions, and porosity.

6.2. Wellbore Microannulus

The characterization of wellbore integrity is critical for use as long-term subsurface storage reservoirs of CO_2. The wellbore is comprised of two distinct regions, the steel casing, and the cement sheath. The interface between these two regions presents modeling challenges using classical techniques due to dissimilar materials. Simulating crack propagation brings with it a wide variety of challenges as well. Employing the FEM requires the use of special elements like CZ elements and remeshing. The extended FEM presents other difficulties, and both are computationally expensive. Since damage propagation and dissimilar materials are of concern, the use of the peridynamics provides a natural framework to approach wellbore characterization. The wellbore microannulus is caused by the debonding that occurs between the steel and cement regions. The wellbore model is created by having two nested hollow cylinders subjected to internal and external pressure as shown in Fig. 6-5. Cement and streel properties for the peridynamic simulations are included in Table 6-2.

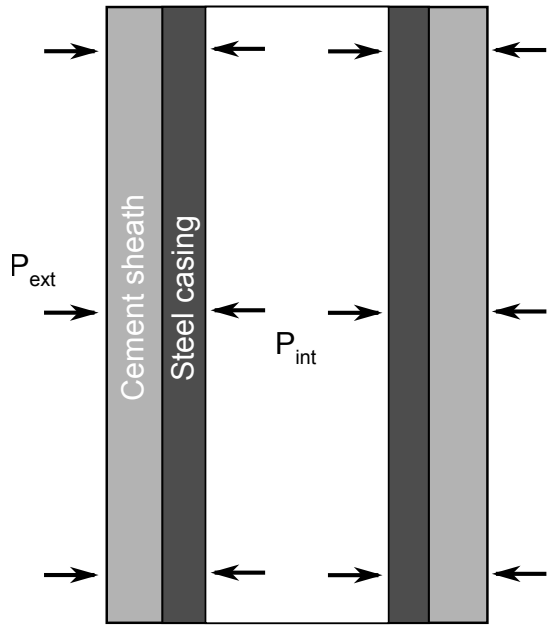

Figure 6-5. Simplified wellbore geometry for evaluation of role of microannulus.

Table 6-2. Cement and steel properties for peridynamic wellbore simulations. [66]

Material	Bulk modulus (GPa)	Shear modulus (GPa)	Critical stretch (m)
Steel	160	78	No failure
Cement	20	12	7.3e-5

Gomez et. al approached this problem using Sierra a FEA software package [66]. This research attempts to recreate their finite element model by creating a similar finite element mesh and then converting it to its peridynamic equivalent. To achieve an error of less than 1% compared to an analytical analysis a model containing 466,000 elements was created [66]. This model does not include any special treatment of the interface between steel and cement as they are considered to be perfectly bonded.

The FEA mesh was converted to a peridynamic mesh by extracting the node and element information. In the case of an 8-node brick element, the centroids were determined and made into the new peridynamic material points. The corresponding element's volume was also assigned to the peridynamic material point. The total number of elements is equivalent to the total number of peridynamic material points.

There is not a direct way to apply the external and internal pressure to the peridynamic model. Therefore, the displacement field from the confining pressure in the FEA analysis is used to determine the boundary conditions. Since this problem is symmetric with respect to loading and geometry, the displacement field is assumed to not have angular dependence. Therefore, the nodal displacements at the inner and outer surfaces are extracted from the FEA model and applied directly as the peridynamic prescribed displacements boundary conditions. Figure 6-6 illustrates the conversion between FE mesh and the peridynamic material point cloud.

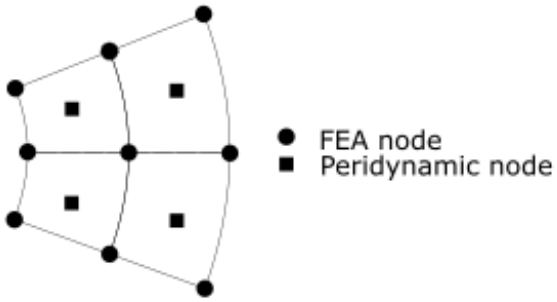

Figure 6-6. FE mesh and corresponding peridynamic material points for modeling wellbore geometries.

As can be seen from Fig. 6-7, the peridynamic material points are always positioned inside FE geometry. To obtain more accurate boundary conditions, the displacements are interpolated at the centroid's position.

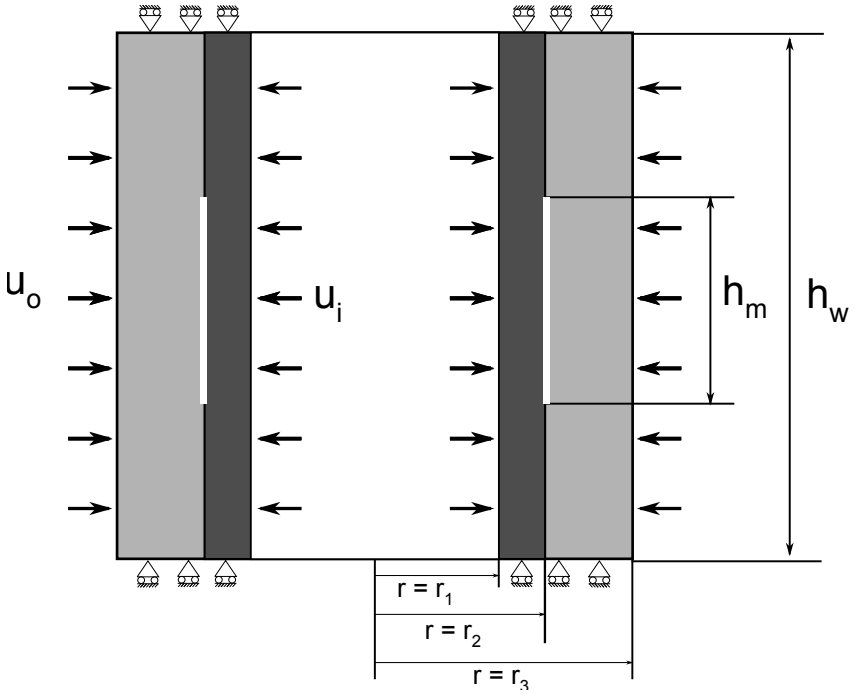

Figure 6-7. Cross-section of peridynamic wellbore problem description

Modeling the cement sheath and steel casing interface is accomplished in a variety of ways. Using Peridigm, an Open source peridynamics based code, the introduction of bond filters to the model can provide users with a region where bonds are initially broken. Peridigm is currently limited to a plane shaped bond filter, however, there is no limit to the number of planes that can be included. The actual wellbore can have a small gap (microannulus) that occurs between the sheath and casing. To model this gap using peridynamic using bond filters would cause no interaction between the sheath and casing. To allow the two domains to interact, the microannuli created through bond filters will not extend through the entire axial length. Three different microannuli will be studied as shown in Figure 6-8. These are the quarter, half, and full microannuli. The microannulus' height remains constant. Peridigm has several solvers for explicit or implicit analysis. This study will focus on the quasistatic solver which uses implicit time integration. Simulations were run for 1.0 s with 100 load steps and a 0.01-time step.

Dimensions and boundary conditions

$r_1 = 24.475\ mm, r_2 = 28.825\ mm, r_3 = 50.8\ mm, h_w = 200\ mm, h_m = 40\ mm$

$u_i(r = 24.475,z,t) = 2.9583 \times 10^{-5}t$

$u_o(r = 50.8,z,t) = -1.765 \times 10^{-4}t$

$u(x,y,z = \pm\ 100,t) = 0$

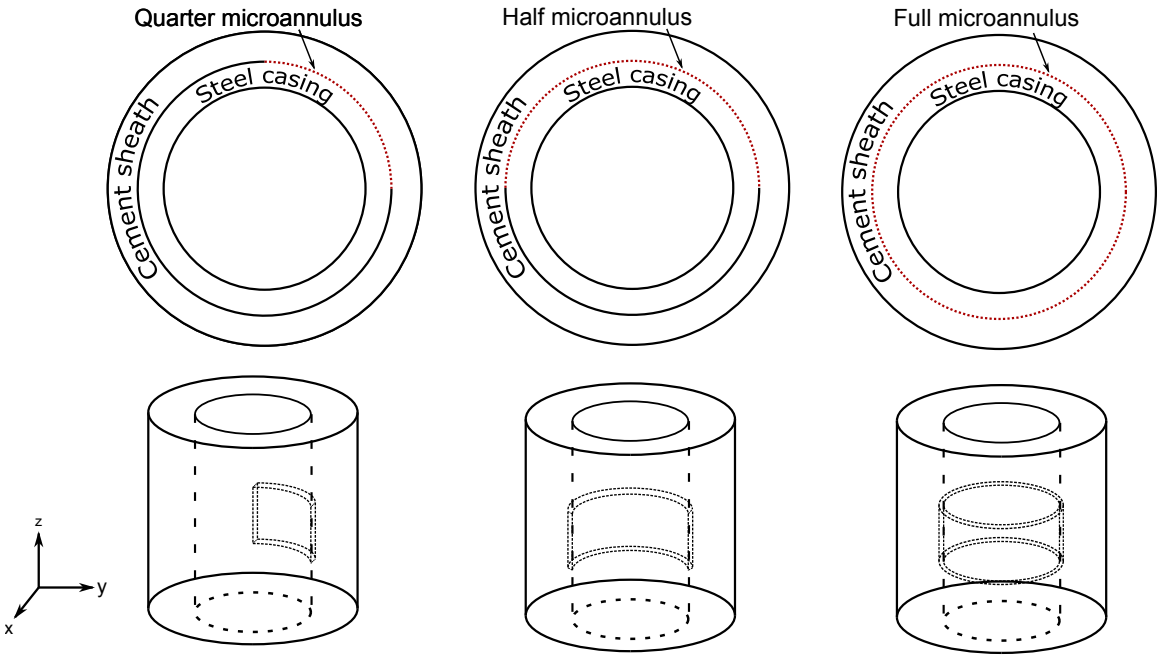

Figure 6-8. Geometries of microannulus geometries in peridynamics borehole simulations.

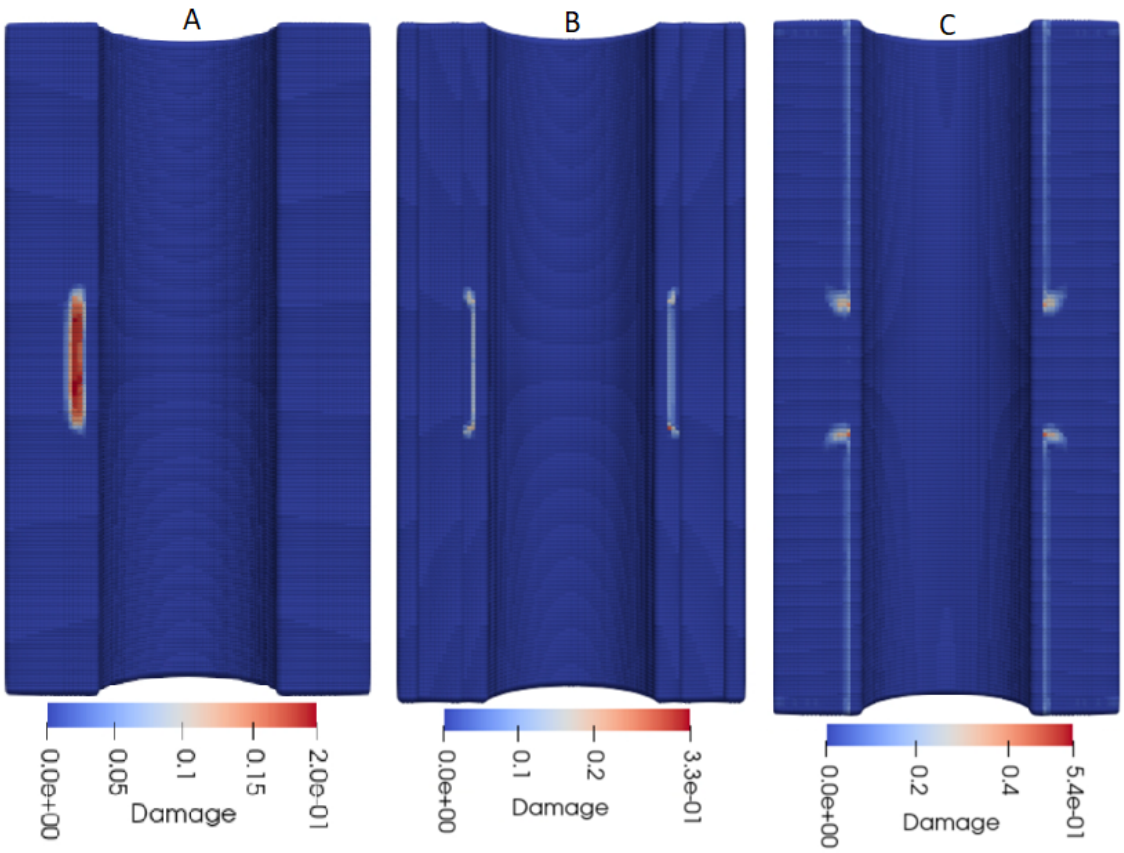

Figure 6-9. Damage variation for quarter (A), half (B), and full (C) microannulus geometries.

Another approach to model the microannulus is to modify the bonds that extend between the casing and sheath. Instead of severing the connection between the two domains completely, the properties of the bonds that pass through the microannulus are adjusted. This avoids modeling an expensive contact simulation and allows the microannulus to extend throughout the wellbore. This also enables the application of boundary conditions that are related to the subsurface movements that wellbore structures may experience. Figure 6-10 depicts a new wellbore problem with the addition of a subsurface layer and different boundary conditions. The top of the wellbore is fixed, and the outer material region is subjected to a linearly varying prescribed displacement constraint. This displacement is meant to simulate a separate layer of subsurface material subjecting the wellbore to shear-type loading. A final time of 365 days was used, with 730 load steps and a time step of 0.5 days. The material properties used in the simulations for the steel, cement, and subsurface rock are included in Table 6-3.

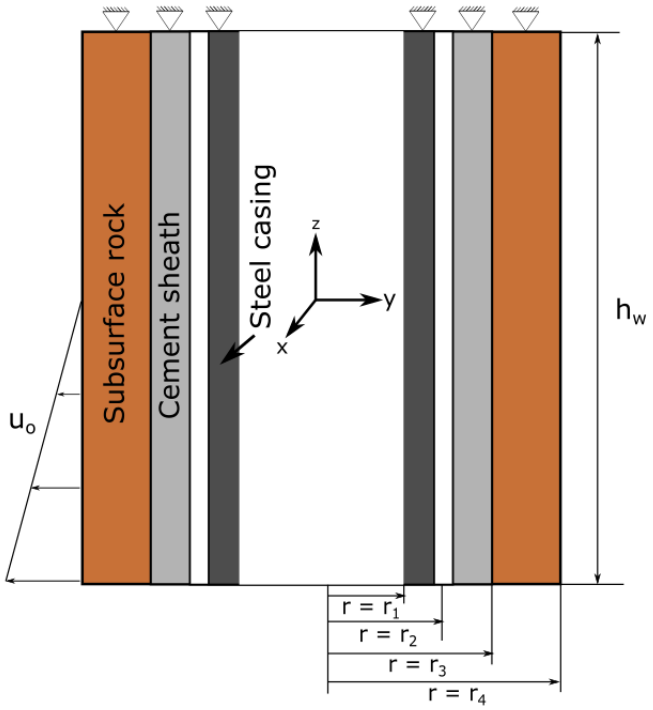

Figure 6-10. Schematic of wellbore model for extended lifetime failure and includes subsurface rock, cement sheath, and steel casing.

Table 6-3. Steel, cement, and subsurface rock properties and failure criteria used in peridynamic simulations of wellbores with subsurface rock [66]

Material	Bulk modulus (GPa)	Shear modulus (GPa)	Critical stretch (m)
Steel	160	78	No failure
Cement	20	12	5.53e-4
Subsurface rock	20	12	No failure

Dimensions and boundary conditions

$r_1 = 24.475\ mm, r_2 = 28.825\ mm, r_3 = 50.8\ mm, r_4 = 60\ mm, h_w = 200\ mm$

$$u_o(x,y,z<0,t) = (2\times10^{-11}t^2 + 2\times10^{-6}t)\frac{|z|}{0.5h_w}$$

$$u\left(x,y,z=\frac{h_w}{2},t\right) = 0$$

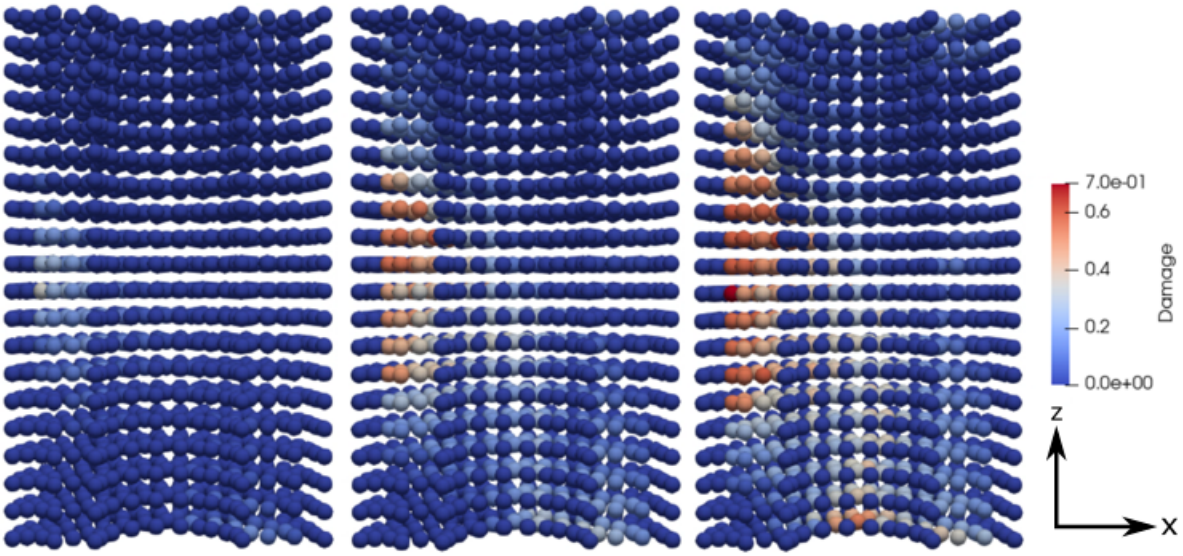

Figure 6-11. Damage propagation in wellbore models as time progresses t = 125, 250, 365 days (left to right)

As can be seen from above, the microannulus region can be constructed using different approaches. There have not been direct comparisons made between modifying bond properties versus the use of bond filters. Extending the bond filters axially would result in no analysis being performed, whereas modifying the interfacial bonds forms a new version of the microannulus. This comparison should be explored further.

Figure 6-10 shows the three different geometries of microannulus created using bond filters. The damage pattern for these cases is shown in Figure 6-11. Most of the damage is seen near the edges of the micro annuli. Note the scale of the damage for (A), (B), and (C) are all different. The quarter geometry exhibits the smallest local damage value ~0.2, which makes sense since the microannulus is impacting the structure much less compared to the full geometry (C). The full geometry shows damage propagate axially through the wellbore structure, which is not seen in the (A) or (B) cases. The half geometry shows a maximum local damage of ~ 0.3 these falls between two extremes (A) and (C).

Modeling the microannulus using modified bond properties allows other types of loading conditions to be studied. The case shown in Figure 6-10 include a subsurface region in which displacement boundary conditions are applied. The displacements vary linearly with a minimum displacement near the center of the wellbore and the maximum occurring at the bottom. Figure 6-11 shows the damage propagation after one year. The critical stretch value plays a large role in the length the simulation can run and the extent of damage. The critical stretch value has been increased to allow the simulation to run longer in order to investigate the damage propagation. As can be seen from Figure 6-11 at around 125 days damage initiates near the center line of the structure. After 250 days, significant damage has occurred in the cement sheath. One thing to note is the there is more damage around $\theta = 180°$ due to the direction of loading being in the positive x-direction $\theta = 0°$. After 365 days the damage has progressed farther axially and circumferentially. A more refined version of this model may provide more insight into the damage mechanisms.

7. CZ MODELING OF CONCRETE HYDRATION

For quasi-brittle porous materials, structural analysis in the presence of pore fluid whereby the pore fluid pressure evolves, cannot be conducted without a fully coupled poromechanical analysis in which the field variables are solid skeleton displacement and pore fluid pressure for a two-field finite element formulation. Special attention is given to pressure-sensitive materials, such as concrete or rocks, since these materials are classified as quasi-brittle materials in which discontinuities, such as cracks, can develop, leading to additional challenges. One challenge is properly accounting for preferential fluid flow inside the discontinuities, and the fluid exchange between the discontinuities and the surrounding bulk porous domain. Another challenge is modeling the CZ crack traction-displacement nonlinear constitutive response within the coupled poromechanical framework.

Coupled poromechanical analysis with discontinuities is crucial to investigating the performance and the stability of civil engineering structures that interact with pore fluids and fluids in cracks. Examples include (i) concrete gravity dams under which base joints can develop due to increasing water levels at the upstream side of the dam, or (ii) hydraulic fracturing by which fluid is injected at high pressure to create cracks in order to extract petroleum or natural gas or extract heat from geothermal reservoirs. In addition, the stability of geologic faults, water reservoirs, and underground gas storage reservoirs can be better understood through coupled poromechanical analysis with discontinuities. Other examples such as slope stability and tunnel safety may also be considered.

In this work, a fully coupled bulk element and CIE poromechanical FEA capability, along with a newly developed simple elastoplastic mode I-II CZ traction-displacement constitutive model, were developed for the analysis of cracking in quasi-brittle fluid-saturated (biphasic) porous media. In the simple elastoplastic CZ traction-displacement constitutive model, tensile strength and cohesion internal state variables evolve, while friction and dilatation angles are assumed to remain constant during the analysis. Other constitutive models include the effective stress principle with standard bulk solid skeleton constitutive model such as linear isotropic elasticity and Drucker-Prager cap plasticity (not implemented), Darcy's law for fluid flow in bulk porous media, and constitutive fluid flow models for the discontinuities.

A simple phenomenological CZ model is developed to investigate crack strength evolution in mode I, which can be extended to include mode II and mixed mode I-II cracking. In the CZ model, crack tensile strength evolves (weakens or strengthens due to CO_2 exposure or concrete hydration, for example) in real time to phenomenologically describe chemical species transport to the discontinuities that contributes to crack strength evolution.

Numerical examples are presented for simple test problems, and for real world examples with either experimental data to calibrate parameters, or larger scale structural analyses such as concrete gravity dam stability. For the experiments, notched and un-notched cement concrete beams at the University of New Mexico are cracked in three-point bend configuration with and without chemistry effects. Also, short rod experiments conducted at Sandia National Laboratories are simulated to calibrate CZ parameters with and without chemistry effects.

An Abaqus user element subroutine is developed to solve the fully coupled poromechanical nonlinear FEA of crack propagation in 2D with two element types: (i) bulk porous continuum element, and (ii) CIE with aperture-dependent fluid flow properties. In addition, an extension to the simple mode I-II CZ model formulation and implementation includes effect of chemistry phenomenologically on tensile strength (strengthening for cement hydration, and weakening for CO_2 degradation, for instance).

Finally, in order to generate the mixed formulation FE meshes, scripts are written making use of the Python interface to the well-known mesh generation software Cubit developed at Sandia

National Laboratories. Specifically, a Python script was developed to generate the 2D FE meshes with poromechanical Q9P4 (biquadratic in solid skeleton displacement, bilinear is pore fluid pressure) elements for bulk porous domains, and poromechanical Q6P4 (quadratic in solid skeleton displacement, linear in pore fluid pressure) CIEs for discontinuous porous domains inserted at bulk element edges.

8. CEMENT PASTE DURABILITY

Current research on concrete durability, longevity, sustainability, and resilience necessitates an understanding of external factors' effect on the long-term degradation of concrete. As cement is the main binder in concrete, understanding cement degradation is critical to understanding concrete degradation. Chemical degradation of Portland cement occurs primarily through three distinct paths: exchange reactions between an aggressive fluid and cementitious compounds, dissolution, and leaching of cementitious compounds, or reactions of cement with other materials that form expansive products. [67, 68] This research is focused on the chemical degradation of cement, not the degradation of concrete as a composite with aggregate and/or reinforcement, excluding common concrete degradation concerns such as an alkali-silica reaction and chloride-ion attack, but focusing on HCP.

The work started by performing a detailed review of the research conducted in this field. A review article [69] was developed and is submitted for publication. Cement degrades due to chemical reactions that cause the overall matrix composition to change from stiff calcium silicates to low stiffness minerals. The primary forms in cement degradation include, but are not limited to, calcium leaching, sulfate attack, carbonation, and chloride penetration. A schematic representation of the four primary forms of cement and concrete degradation is presented in Figure 8-1

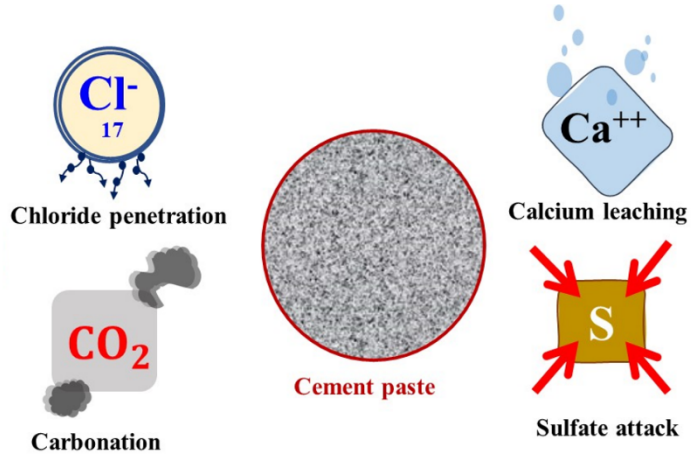

Figure 8-1. Schematic representation of the four primary forms of cement degradation: chloride penetration, carbonation, calcium leaching, and sulfate attack [69]

The mechanical testing in this campaign was performed on cement paste samples with a water/cement ratio of 0.45, with dimensions 150 mm x 25 mm x 25 mm (L x W x D) as shown in Figure 8-2, meeting ACI 446 fracture testing guidelines. [70] Twenty-four hours after casting, samples were demolded and moved to a curing room where the humidity is 99% R.H. where samples were allowed to cure for 6 additional days. Fracture samples had notches of depth 8.3 mm and width of 0.3 mm. Un-notched samples were also tested to determine flexural strength. Schematic of the notched test specimens are shown in Figure 8-2

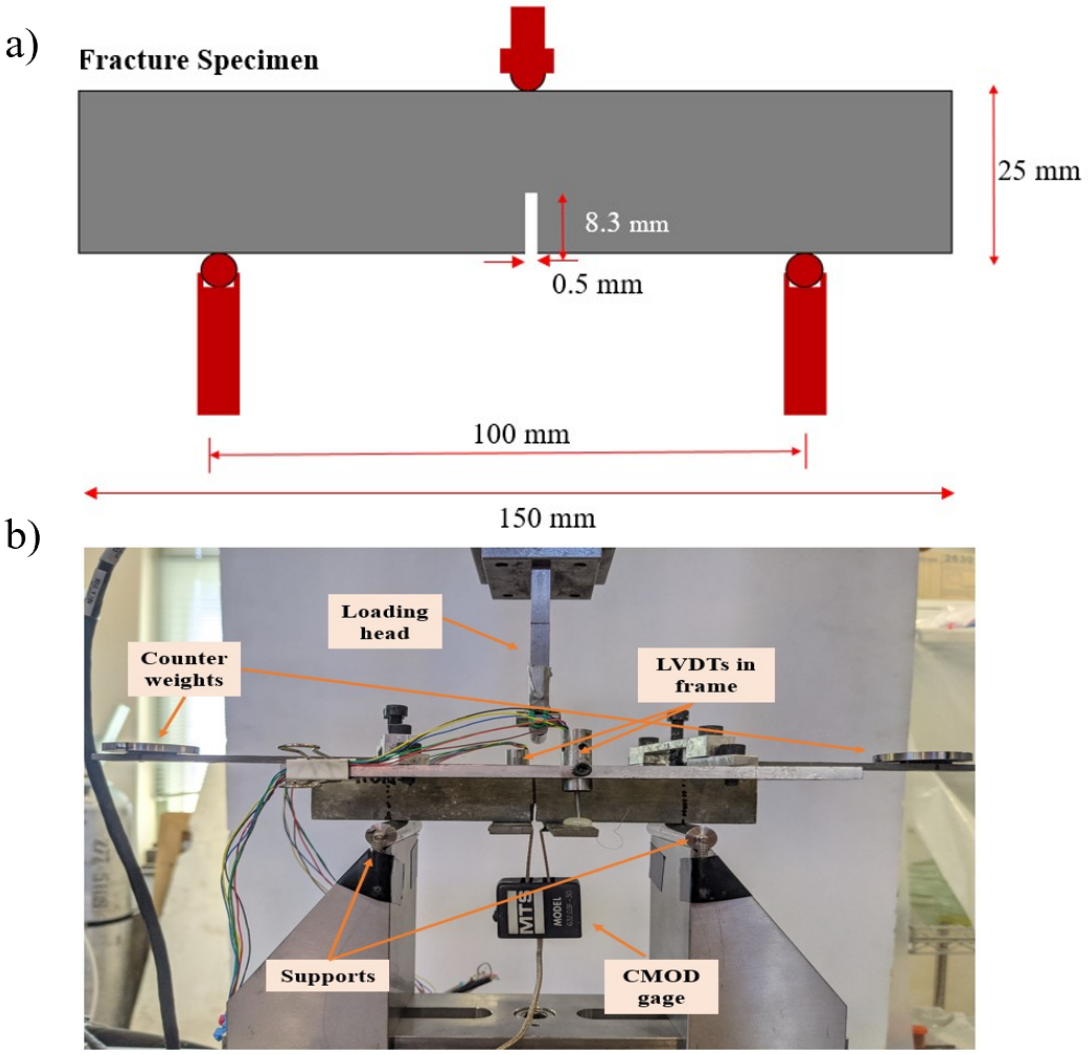

Figure 8-2. (a) Schematic and (b) test setup of cement paste fracture test using three-point bending.

Once the samples were properly prepared and initial dimension and weight measurements had been taken, they were placed into their respective degradation mode – neat, calcium leaching, or sulfate attack. The neat samples were placed back into the curing room. The calcium leaching samples were placed into an ammonium nitrate (NH_4NO_3) solution bath with a concentration of 480 g/L (6 M). The sulfate attack samples were placed into a sodium sulfate (Na_2SO_4) bath with a concentration of 50 g/L (0.35 M). The specimens were exposed to R.H. of 16%, 50%, or 99% the day before testing for each category. The apparent mechanical and fracture properties were determined from testing the samples at 1-, 12-, and 24- weeks of exposure. Example degradation tanks are shown in Figure 8-3. Example damaged cement samples during exposure to degradation environments are shown in Figure 8-4.

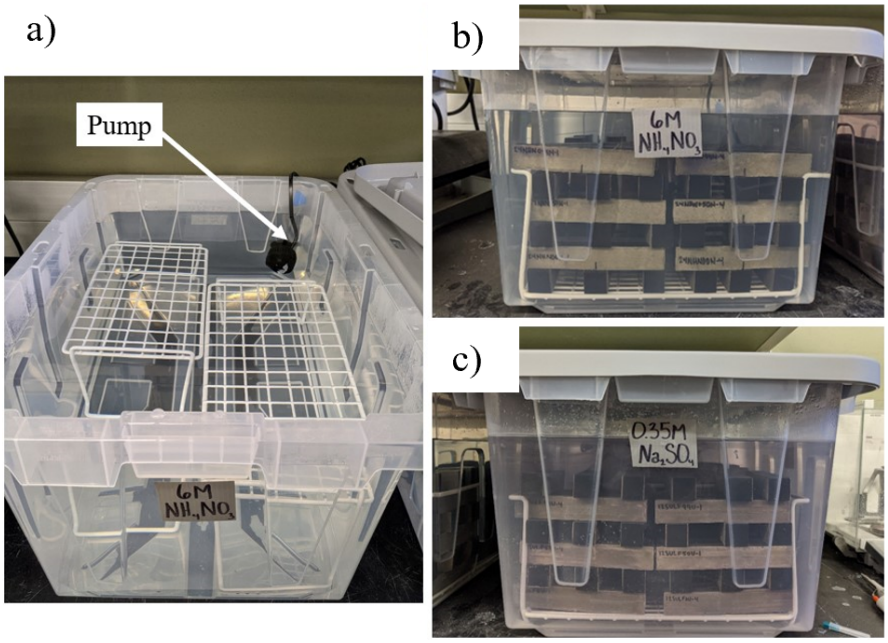

Figure 8-3. Degradation environment a) bath with no samples. b) and c) Two degradation baths for calcium leaching and sulfate attack with samples.

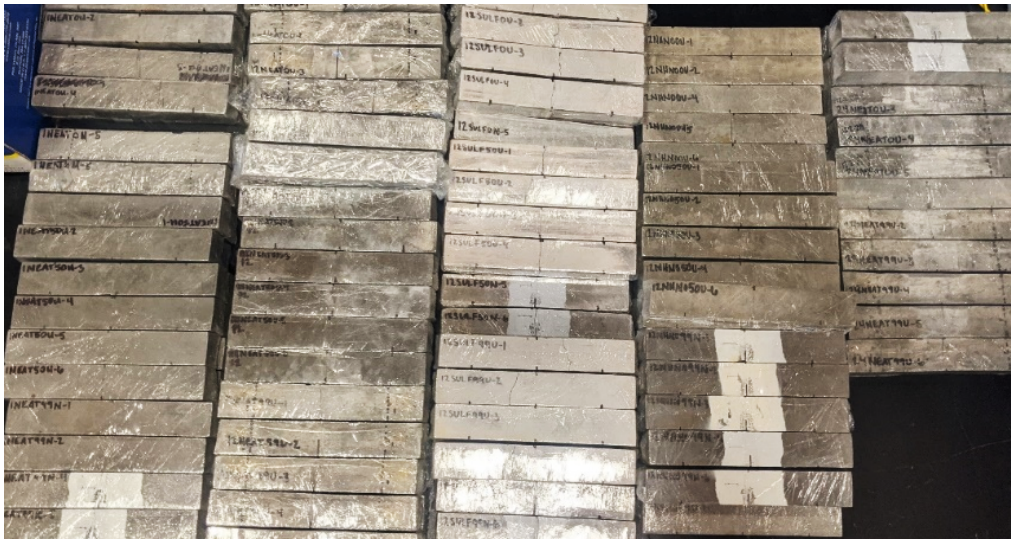

Figure 8-4. Samples degradation at different exposure time showing the significance of degradation on the external color and appearance of cement paste.

From the tested specimens, a 10-20 mg piece was tested in the thermal gravimetric analysis (TGA) equipment using a heating rate of 20°C/min up to 800°C with an airflow of nitrogen at 40 ml/min. TGA is a microstructural analysis method that supplements the visual readings and provide a specific information of the chemical compounds of the cementitious matrix using thermal analysis.

Figure 8-5. shows a sample of the results for degradation at 12-weeks of exposure. Across the 99% RH exposure, the stiffness, modulus of rupture, and fracture energy are all greatly lessened in both degradation exposures. More details about the experimental campaign and results could be found in Ref: [71]

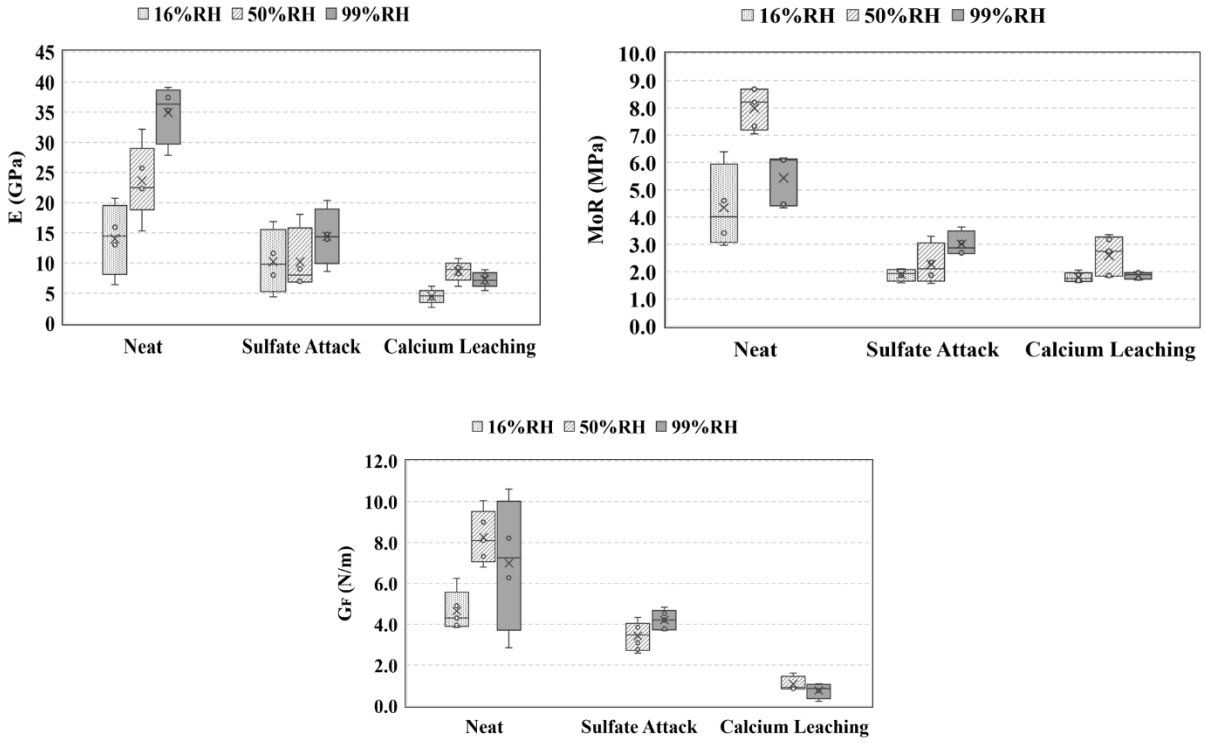

Figure 8-5. Summary data for modulus of elasticity, modulus of rupture, and fracture energy after 12-weeks of exposure to degrading environment

The results from both notched and unnotched specimens were used to evaluate the mechanical and fracture properties and their change with each degradation level. At first glance, the effect of degradation on both moduli of elasticity and modulus of rupture could be observed. The more the specimen is degraded, the less value of each modulus it had. Moreover, the calcium leaching sample at investigated concentration consistently showed lower values than the sulfur attack samples. The effect of relative humidity before testing did not show a statistical significance within the same degradation level. For the fracture energy, the neat samples had the highest values, the sulfate attack samples had the second highest, and the calcium leached samples exhibited the lowest values for both G_{IC} and J_{IC}. It is important to note that J_{IC} may be inconsistent as it reflects plastic behavior. As observed in this study, cement paste was a very brittle, linear elastic material with little to no plastic behavior.

The results of the TGA tests performed on the 12-week exposure samples reflected the presence of main binding compounds to different extents. For the neat results, all depths observed peaks ~100°C (where the evaporable water, ettringite, and gypsum are decomposed) and between 400-500°C (where calcium hydroxide (CH) is dehydroxylated). The minor peak observed just below 400°C can be attributed to carboaluminate phases decomposing. Some tests observed a smaller peak between 650-900°C. It is reported decarbonation of calcium carbonate occurs at this temperature range. [72] For sulfate attack samples, it can be observed that the sulfate attack samples have sharper,

more intense initial peaks of ~100°C. This can be explained by the mechanism behind the sulfate attack; sulfate attack leads to a new formation of ettringite, which is the compound lost at this temperature. Besides this first peak, the sulfate attack curves are very similar to the neat samples. For calcium leached samples, two predominant peaks are observed at each depth (at ~100°C and ~475°C), with a third minor peak just above 300°C. The results from the edge also exhibit a notable peak at ~675°C. At first glance, the TGA tests seem to reflect the potential presence of important binding compounds, as with the neat and sulfate attack experiments. This can be explained by the similarity between the decomposition of calcium nitrate and the decomposition of binding compounds. Since CH is dehydroxylated between 400-500°C, which overlaps with the decomposition of calcium nitrate between 450-650°C [72], it would be reasonable to attribute these similar dominant peaks, that seemingly show the presence of binding compounds, to reflect the presence of calcium nitrate in the leached matrix.

Cement paste samples were degraded, monitored, tested, and evaluated to observe the degradation environment and relative humidity effects on cement fracture. Degradation baths were renewed regularly, and sample density change was observed over time. Calcium leaching reduced sample density by 18.8% after 20 weeks of exposure. This proved to be severe that samples exhibited visible cracks from degradation, and it was determined that calcium leached samples were unable to be tested beyond 12-weeks of exposure. Fracture and flexure tests for varying degradation environments and relative humidity were performed to quantify the significance of these environments on the degradation of cement. Mechanical properties, including the modulus of rupture and modulus of elasticity and fracture characteristics, including elastic and elastic-plastic fracture toughness parameters, were determined. The results show the effect leaches out calcium-rich compounds over time on the integrity of the cementitious matrix, yielding an obvious reduction in the mechanical and fracture properties. On the other hand, the formation of ettringite due to sulfate attack caused expansion and high internal stresses, which in turn derived internal cracking, causing apparent degradation in the cementitious matrix.

Future work could include testing at later ages to better understand the complicated nature of cement degradation as exposure time changes. Since the calcium leached samples become over leached beyond 12-weeks of exposure in these conditions, it might be important to consider testing at the earlier exposure times as this would give crucial insight into the evolving effect of degradation of the cementitious matrix due to calcium leaching. Future work might also include chemical and microstructural investigations of the sulfate attack, and calcium leached degraded samples up to 12-weeks of age. Another area of interest would be to devise a testing scheme to evaluate degradation and relative humidity in parallel rather than in series, as they were applied in this study.

REFERENCES

[1] S.E. Gasda, S. Bachu, M.A. Celia, Spatial characterization of the location of potentially leaky wells penetrating a deep saline aquifer in a mature sedimentary basin, Environ. Geol. 46(6-7) (2004) 707-720.
[2] C.C.M. Andreson, Larry Mogck, Bitsy Cohen, Gregg Scott Concrete Dams Case Histories and Failures and Nonfailures with Back Calcuations, (1999) 100.
[3] A.K. Chopra, J.T. Wang, Earthquake response of arch dams to spatially varying ground motion, Earthquake Eng. Struct. Dyn. 39(8) (2010) 887-906.
[4] T. Ngo, P. Mendis, A. Gupta, J. Ramsay, Blast loading and blast effects on structures–an overview, Electron. J. Struct. Eng. 7(S1) (2007) 76-91.
[5] B. Lawn, Fracture of brittle solids, Cambridge university press1993.
[6] B. Saassouh, Z. Lounis, Probabilistic modeling of chloride-induced corrosion in concrete structures using first-and second-order reliability methods, Cem. Concr. Compos. 34(9) (2012) 1082-1093.
[7] X. Zhu, G. Zi, W. Lee, S. Kim, J. Kong, Probabilistic analysis of reinforcement corrosion due to the combined action of carbonation and chloride ingress in concrete, Construction and Building Materials 124 (2016) 667-680.
[8] M. Elices, G. Guinea, J. Gomez, J. Planas, The cohesive zone model: advantages, limitations and challenges, Eng. Fract. Mech. 69(2) (2002) 137-163.
[9] G. Guinea, J. Planas, M. Elices, A general bilinear fit for the softening curve of concrete, Mater. Struct. 27(2) (1994) 99-105.
[10] H. Kim, M.P. Wagoner, W.G. Buttlar, Numerical fracture analysis on the specimen size dependency of asphalt concrete using a cohesive softening model, Construction and Building Materials 23(5) (2009) 2112-2120.
[11] K. Park, G.H. Paulino, J. Roesler, Cohesive fracture model for functionally graded fiber reinforced concrete, Cem. Concr. Res. 40(6) (2010) 956-965.
[12] K. Park, G.H. Paulino, J.R. Roesler, Determination of the kink point in the bilinear softening model for concrete, Eng. Fract. Mech. 75(13) (2008) 3806-3818.
[13] J. Roesler, G.H. Paulino, K. Park, C. Gaedicke, Concrete fracture prediction using bilinear softening, Cem. Concr. Compos. 29(4) (2007) 300-312.
[14] J. Wang, Cohesive zone model of FRP-concrete interface debonding under mixed-mode loading, IJSS 44(20) (2007) 6551-6568.
[15] M.W. McClure, R.N. Horne, Discrete fracture network modeling of hydraulic stimulation: Coupling flow and geomechanics, Springer Science & Business Media2013.
[16] S. Kelkar, S. Karra, G. Zyvoloski, R. Pawar, S. Rapaka, Coupled Plastic Failure And Permeability In Rocks: a Modeling Approach, 46th US Rock Mechanics/Geomechanics Symposium, American Rock Mechanics Association, 2012.
[17] J.G. Kim, M.D. Deo, Finite element, discrete-fracture model for multiphase flow in porous media, AICHE J. 46(6) (2000) 1120-1130.
[18] M.-C. Cacas, E. Ledoux, G.d. Marsily, B. Tillie, A. Barbreau, E. Durand, B. Feuga, P. Peaudecerf, Modeling fracture flow with a stochastic discrete fracture network: calibration and validation: 1. The flow model, WRR 26(3) (1990) 479-489.
[19] S. Wessling, R. Junker, J. Rutqvist, D. Silin, H. Sulzbacher, T. Tischner, C.-F. Tsang, Pressure analysis of the hydromechanical fracture behaviour in stimulated tight sedimentary geothermal reservoirs, Geoth 38(2) (2009) 211-226.
[20] T.T. Cladouhos, M. Clyne, M. Nichols, S. Petty, W.L. Osborn, L. Nofziger, Newberry Volcano EGS demonstration stimulation modeling, AltaRock Energy, Inc., Seattle, WA, 2011.

[21] S.A. Silling, E. Askari, A meshfree method based on the peridynamic model of solid mechanics, Computers & structures 83(17-18) (2005) 1526-1535.
[22] D.J. Littlewood, S.A. Silling, J.A. Mitchell, P.D. Seleson, S.D. Bond, M.L. Parks, D.Z. Turner, D.J. Burnett, J. Ostien, M. Gunzburger, Strong local-nonlocal coupling for integrated fracture modeling, Sandia Report SAND2015-7998, Sandia National Laboratories 3 (2015).
[23] F. Bobaru, W. Hu, The meaning, selection, and use of the peridynamic horizon and its relation to crack branching in brittle materials, IJFr 176(2) (2012) 215-222.
[24] Y.D. Ha, F. Bobaru, Studies of dynamic crack propagation and crack branching with peridynamics, IJFr 162(1-2) (2010) 229-244.
[25] Y.D. Ha, F. Bobaru, Characteristics of dynamic brittle fracture captured with peridynamics, Eng. Fract. Mech. 78(6) (2011) 1156-1168.
[26] H. Ouchi, A. Katiyar, J. Foster, M.M. Sharma, A peridynamics model for the propagation of hydraulic fractures in heterogeneous, naturally fractured reservoirs, SPE Hydraulic Fracturing Technology Conference, Society of Petroleum Engineers, 2015.
[27] E. Askari, F. Bobaru, R. Lehoucq, M. Parks, S. Silling, O. Weckner, Peridynamics for multiscale materials modeling, Journal of Physics: Conference Series, IOP Publishing, 2008, p. 012078.
[28] B. Alali, R. Lipton, Multiscale dynamics of heterogeneous media in the peridynamic formulation, JElas 106(1) (2012) 71-103.
[29] A. Agwai, I. Guven, E. Madenci, Predicting crack propagation with peridynamics: a comparative study, IJFr 171(1) (2011) 65.
[30] H. Ouchi, A. Katiyar, J. York, J.T. Foster, M.M. Sharma, A fully coupled porous flow and geomechanics model for fluid driven cracks: a peridynamics approach, CompM 55(3) (2015) 561-576.
[31] W. Gerstle, N. Sau, S. Silling, Peridynamic modeling of plain and reinforced concrete structures, (2005).
[32] W. Gerstle, N. Sau, S. Silling, Peridynamic modeling of concrete structures, NuEnD 237(12-13) (2007) 1250-1258.
[33] D.J. Littlewood, K. Mish, K. Pierson, Peridynamic simulation of damage evolution for structural health monitoring, ASME 2012 International Mechanical Engineering Congress and Exposition, American Society of Mechanical Engineers, 2012, pp. 1-8.
[34] R.W. Macek, S.A. Silling, Peridynamics via finite element analysis, Finite Elements in Analysis and Design 43(15) (2007) 1169-1178.
[35] W. Hu, Y.D. Ha, F. Bobaru, Peridynamic model for dynamic fracture in unidirectional fiber-reinforced composites, CMAME 217 (2012) 247-261.
[36] M.L. Parks, R.B. Lehoucq, S.J. Plimpton, S.A. Silling, Implementing peridynamics within a molecular dynamics code, CoPhC 179(11) (2008) 777-783.
[37] D.J. Littlewood, Simulation of dynamic fracture using peridynamics, finite element modeling, and contact, ASME 2010 International Mechanical Engineering Congress and Exposition, American Society of Mechanical Engineers, 2010, pp. 209-217.
[38] P.M. Dove, Geochemical controls on the kinetics of quartz fracture at subcritical tensile stresses, Journal of Geophysical Research: Solid Earth 100(B11) (1995) 22349-22359.
[39] A. Ingraffea, R. Santoro, S. Shonkoff, Wellbore Integrity: Failure Mechanisms, Historical Record, and Rate Analysis. EPA's Study Hydraul. Fract. Its Potential Impact Drink, Water Resour (2013).
[40] E.A. Bradshaw, Deepwater, deep ties, deep trouble: A state-corporate environmental crime analysis of the 2010 Gulf of Mexico oil spill, Western Michigan University2012.
[41] C.L. Sorrensen, A history of transboundary storm water flows: flooding, tunnels, and the spatial incongruity of the US–Mexico border, Journal of Historical Geography 38(4) (2012) 447-457.

[42] J.L. Llopis, J.B. Dunbar, L.D. Wakeley, M.K. Corcoran, D.K. Butler, Tunnel detection along the southwest US border, 18th EEGS Symposium on the Application of Geophysics to Engineering and Environmental Problems, 2005.
[43] L.L. Price, A. Alsaed, Preliminary Analysis of Postclosure DPC Criticality Consequences, Sandia National Lab.(SNL-NM), Albuquerque, NM (United States); Oak Ridge …, 2020.
[44] S.A. Silling, M. Epton, O. Weckner, J. Xu, E. Askari, Peridynamic states and constitutive modeling, Journal of Elasticity 88(2) (2007) 151-184.
[45] J. Trageser, P. Seleson, Bond-based peridynamics: A tale of two Poisson's ratios, Journal of Peridynamics and Nonlocal Modeling 2(3) (2020) 278-288.
[46] S.A. Silling, Reformulation of elasticity theory for discontinuities and long-range forces, J. Mech. Phys. Solids 48(1) (2000) 175-209.
[47] R. Jones, J. Rimsza, J. Trageser, J. Hogancamp, Simulation of cement degradation and estimation of uncertainty in predicted failure times with peridynamics, (2020).
[48] H. Du, S. Dai Pang, High-performance concrete incorporating calcined kaolin clay and limestone as cement substitute, Construction and Building Materials 264 (2020) 120152.
[49] X. Gao, S. Kawashima, X. Liu, S.P. Shah, Influence of clays on the shrinkage and cracking tendency of SCC, Cement and Concrete Composites 34(4) (2012) 478-485.
[50] S. Afzal, K. Shahzada, M. Fahad, S. Saeed, M. Ashraf, Assessment of early-age autogenous shrinkage strains in concrete using bentonite clay as internal curing technique, Construction and Building Materials 66 (2014) 403-409.
[51] E.C. Gaucher, P. Blanc, Cement/clay interactions–a review: experiments, natural analogues, and modeling, Waste Management 26(7) (2006) 776-788.
[52] A. Palomo, M.T. Blanco-Varela, M. Granizo, F. Puertas, T. Vazquez, M. Grutzeck, Chemical stability of cementitious materials based on metakaolin, Cement and Concrete Research 29(7) (1999) 997-1004.
[53] A. Shafizadeh, T. Gimmi, L. Van Loon, A. Kaestner, U. Mäder, S. Churakov, Time-resolved porosity changes at cement-clay interfaces derived from neutron imaging, Cement and concrete research 127 (2020) 105924.
[54] P. Blanc, P. Vieillard, H. Gailhanou, S. Gaboreau, N. Marty, F. Claret, B. Madé, E. Giffaut, ThermoChimie database developments in the framework of cement/clay interactions, Applied Geochemistry 55 (2015) 95-107.
[55] L. De Windt, D. Pellegrini, J. Van Der Lee, Coupled modeling of cement/claystone interactions and radionuclide migration, Journal of Contaminant Hydrology 68(3-4) (2004) 165-182.
[56] N.C. Marty, O. Bildstein, P. Blanc, F. Claret, B. Cochepin, E.C. Gaucher, D. Jacques, J.-E. Lartigue, S. Liu, K.U. Mayer, Benchmarks for multicomponent reactive transport across a cement/clay interface, Computational Geosciences 19(3) (2015) 635-653.
[57] N.C. Marty, I. Munier, E.C. Gaucher, C. Tournassat, S. Gaboreau, C.Q. Vong, E. Giffaut, B. Cochepin, F. Claret, Simulation of cement/clay interactions: feedback on the increasing complexity of modelling strategies, Transport in porous media 104(2) (2014) 385-405.
[58] N.C. Marty, C. Tournassat, A. Burnol, E. Giffaut, E.C. Gaucher, Influence of reaction kinetics and mesh refinement on the numerical modelling of concrete/clay interactions, Journal of Hydrology 364(1-2) (2009) 58-72.
[59] G. Kosakowski, U. Berner, The evolution of clay rock/cement interfaces in a cementitious repository for low-and intermediate level radioactive waste, Physics and Chemistry of the Earth, Parts A/B/C 64 (2013) 65-86.
[60] M. Arroyo, M. Ciantia, R. Castellanza, A. Gens, R. Nova, Simulation of cement-improved clay structures with a bonded elasto-plastic model: A practical approach, Computers and Geotechnics 45 (2012) 140-150.

[61] K. Liu, J.J. Sheng, Z. Zhang, A simulation study of the effect of clay swelling on fracture generation and porosity change in shales under stress anisotropy, Engineering Geology 278 (2020) 105829.
[62] M.N. Islam, A.P. Bunger, N. Huerta, R. Dilmore, Bentonite extrusion into near-borehole fracture, Geosciences 9(12) (2019) 495.
[63] E. Hardin, L.L. Price, E.A. Kalinina, T. Hadgu, A.G. Ilgen, C.R. Bryan, J.M. Scaglione, K. Banerjee, J. Clarity, R. Jubin, Summary of investigations on technical feasibility of direct disposal of dual-purpose canisters, Sandia National Lab.(SNL-NM), Albuquerque, NM (United States); Sandia …, 2015.
[64] A.S. Wagh, Chemically bonded phosphate ceramics: twenty-first century materials with diverse applications, Elsevier2016.
[65] M.J. Rigali, Progress Report on DPC Cement Filler Development, Sandia National Lab.(SNL-NM), Albuquerque, NM (United States), 2021.
[66] S.P. Gomez, S.R. Sobolik, E.N. Matteo, M.R. Taha, J.C. Stormont, Investigation of wellbore microannulus permeability under stress via experimental wellbore mock-up and finite element modeling, Computers and Geotechnics 83 (2017) 168-177.
[67] P.K. Mehta, P.J. Monteiro, Concrete: microstructure, properties, and materials, McGraw-Hill Education2014.
[68] J.F. Young, A. Bentur, S. Mindess, The science and technology of civil engineering materials, (1998).
[69] P. Raby, J. Rimsza, M. Abdellatef, J.U. Stormont, M.U. Taha, Cement Degradation Methods: A Comparative Review, (2021).
[70] W. Gerstle, Progress in developing a standard fracture toughness test for concrete, Structures Congress 2010, 2010, pp. 1915-1926.
[71] P. Raby, Effect of Degradation Environment and Relative Humidity on Fracture of Cement, Civil Engineering, University of New Mexico 2021.
[72] Q.T. Phung, N. Maes, S. Seetharam, Pitfalls in the use and interpretation of TGA and MIP techniques for Ca-leached cementitious materials, Materials & Design 182 (2019) 108041.

DISTRIBUTION

Email—Internal

Name	Org.	Sandia Email Address
David Littlewood	1444	djlittl@sandia.gov
Jeremy Trageser	1444	jtrages@sandia.gov
Stewart Silling	1444	sasilli@sandia.gov
Joshua Hogancamp	5421	jgohanc@sandia.gov
Reese Jones	8363	rjones@sandia.gov
Jakob Ostien	8363	jtostie@sandia.gov
Matthew Sumner	8714	msumne@sandia.gov
Russell Camphouse	8842	rccamph@sandia.gov
Edward Matteo	8842	enmatte@sandia.gov
Chven Mitchell	8842	camitc@sandia.gov
Geoffrey Freeze	8843	gafreez@sandia.gov
Mark Rigali	8843	mjrigal@sandia.gov
Donald Conley	8912	dconley@sandia.gov
Anna Lord	8912	acsnide@sandia.gov
Steven Sobolik	8912	srsobol@sandia.gov
Hongyou Fan	8915	hfan@sandia.gov
Cody Mitts	8915	cmitts@sandia.gov
Jessica Rimsza	8915	jrimsza@sandia.gov
Christa Torrence	8915	cetorre@sandia.gov
Cliff Ho	8920	ckho@sandia.gov
Technical Library	01977	sanddocs@sandia.gov

Email—External [redacted]

Name	Company Email Address	Company Name
Laura Pyrak-Nolte	ljpn@purdue.edu	Purdue University
Richard Regueiro	Richard.regueiro@coloardo.edu	University of Colorado, Boulder
Mahmoud Reda Taha	mrtaha@unm.edu	University of New Mexico

Hardcopy—Internal

Number of Copies	Name	Org.	Mailstop
1	Donald Conley	8912	0750
1	Jessica Rimsza	8915	0750

This page left blank

This page left blank

Sandia National Laboratories

Sandia National Laboratories is a multimission laboratory managed and operated by National Technology & Engineering Solutions of Sandia LLC, a wholly owned subsidiary of Honeywell International Inc. for the U.S. Department of Energy's National Nuclear Security Administration under contract DE-NA0003525.